

This discussion paper is/has been under review for the journal Atmospheric Measurement Techniques (AMT). Please refer to the corresponding final paper in AMT if available.

A new stratospheric and tropospheric NO₂ retrieval algorithm for nadir-viewing satellite instruments: applications to OMI

E. J. Bucsela¹, N. A. Krotkov², E. A. Celarier^{2,3}, L. N. Lamsal^{2,3}, W. H. Swartz^{2,4},
P. K. Bhartia², K. F. Boersma^{5,6}, J. P. Veefkind⁵, J. F. Gleason², and
K. E. Pickering²

¹SRI International, Menlo Park, CA 94025, USA

²Laboratory for Atmospheres, NASA Goddard Space Flight Center, Greenbelt, MD 20771, USA

³Universities Space Research Association, Columbia, MD 21044, USA

⁴Applied Physics Laboratory, The Johns Hopkins University, Laurel, MD 20723, USA

⁵Royal Netherlands Meteorological Institute, De Bilt, The Netherlands

⁶Eindhoven University of Technology, Eindhoven, The Netherlands

Received: 20 November 2012 – Accepted: 8 January 2013 – Published: 7 February 2013

Correspondence to: E. J. Bucsela (bucsela@ix.netcom.com)

Published by Copernicus Publications on behalf of the European Geosciences Union.

Title Page

Abstract

Introduction

Conclusions

References

Tables

Figures

◀

▶

◀

▶

Back

Close

Full Screen / Esc

Printer-friendly Version

Interactive Discussion



Abstract

We describe a new algorithm for the retrieval of nitrogen dioxide (NO_2) vertical columns from nadir-viewing satellite instruments. This algorithm (SP2) is the basis for the Version 2.1 OMI NO_2 Standard Product and features a novel method for separating the stratospheric and tropospheric columns. The approach estimates the stratospheric NO_2 directly from satellite data without using stratospheric chemical transport models or assuming any global zonal wave pattern. Tropospheric NO_2 columns are retrieved using air mass factors derived from high-resolution radiative transfer calculations and a monthly climatology of NO_2 profile shapes. We also present details of how uncertainties in the retrieved columns are estimated. The sensitivity of the retrieval to assumptions made in the stratosphere-troposphere separation is discussed and shown to be small, in an absolute sense, for most regions. We compare daily and monthly mean global OMI NO_2 retrievals using the SP2 algorithm with those of the original Version 1 Standard Product (SP1) and the Dutch DOMINO product. The SP2 retrievals yield significantly smaller summertime tropospheric columns than SP1 and are relatively free of modeling artifacts and negative tropospheric NO_2 values. In a re-analysis of an INTEX-B validation study, we show that SP2 largely eliminates a $\sim 20\%$ discrepancy that existed between OMI and independent in situ springtime NO_2 SP1 measurements.

1 Introduction

Nitrogen oxides are important atmospheric trace gases that have significant impacts on human health. The two principal nitrogen oxides, nitric oxide (NO) and nitrogen dioxide (NO_2) (collectively, NO_x), play key roles in atmospheric aerosol formation and tropospheric ozone chemistry. Major sources of tropospheric NO_x include combustion, soil emissions, and lightning. In the lower troposphere, NO_2 is a toxic gas and a precursor to tropospheric ozone through the reaction of NO_x with volatile organic compounds (VOCs). In the stratosphere, NO_x contributes to both production and loss cycles of

AMTD

6, 1361–1407, 2013

Applications to OMI

E. J. Bucsela et al.

Title Page

Abstract

Introduction

Conclusions

References

Tables

Figures

◀

▶

◀

▶

Back

Close

Full Screen / Esc

Printer-friendly Version

Interactive Discussion



Applications to OMI

E. J. Bucsela et al.

ozone and may indicate long-term changes in tropospheric emissions of nitrous oxide (N_2O), an important greenhouse gas. Stratospheric NO_x is produced mainly by the reaction of N_2O with $\text{O}(^1\text{D})$.

NO_2 has an easily observable spectral signature with strong spectral absorption lines in the visible, infrared, and near ultraviolet. In particular, its broad, highly structured absorption feature in the blue-violet range can be exploited for remote sensing (Platt and Perner, 1983; Platt, 1994). Early spectroscopic ground-based measurements of NO_2 were described by Brewer et al. (1973), Noxon (1975), and Solomon and Garcia (1984). Global retrievals from satellite spectra became available beginning in the middle 1990s, including measurements by the Global Ozone Monitoring Experiment (GOME) instrument (1995–2003) (Burrows et al., 1999b), continued by the Scanning Imaging Spectrometer for Atmospheric Cartography (SCIAMACHY) instrument (2002–2012) (Bovensmann et al., 1999), and currently by the Ozone Monitoring Instrument (OMI) (Levelt et al., 2006; Bucsela et al., 2006; Boersma et al., 2007, 2011) and GOME-2 (Callies et al., 2000; Valks and Loyola, 2008; Valks et al., 2011) instruments.

Satellite and in situ measurements of tropospheric nitrogen oxides are used with chemical transport models (CTMs) to quantify sources and transport of NO_2 pollution from power plants, automobiles, ships, and aircraft (e.g., Martin et al., 2003, 2006; Zhang et al., 2007; Beirle et al., 2004, 2011; Jaegle et al., 2005; Frost et al., 2006; Boersma et al., 2008; Lin et al., 2010; Russell et al., 2010). Instruments on satellite platforms are particularly valuable, since they can obtain NO_2 measurements over large geographical regions. Top-down NO_2 measurements are helpful in constraining emissions for global- and regional-scale atmospheric models (Martin et al., 2003; Choi et al., 2008; Lamsal et al., 2010). Multiyear, consistent time-series measurements allow the study of inter-annual variability and long-term trends (Richter et al., 2005), which have been used to assess the effectiveness of emission control regulations and the effects of economic trends on industrial activity (Frost et al., 2006; Kim et al., 2006; Castellanos and Boersma, 2012). NO_x produced by lightning (LNO_x) contributes an additional 10–15 % to total NO_x production in the troposphere (Schumann and Huntrieser,

Title Page

Abstract

Introduction

Conclusions

References

Tables

Figures

◀

▶

◀

▶

Back

Close

Full Screen / Esc

Printer-friendly Version

Interactive Discussion



2007), and LNO_x measurements are helpful in estimating the global NO_x budget (Tie et al., 2002; Martin et al., 2007).

In unpolluted areas, the stratospheric NO₂ can exceed 90 % of the total NO₂ column (Martin et al., 2002). The partitioning of NO_x and NO_y in the stratosphere is sensitive to photochemical conditions; thus, NO₂ has a strong diurnal dependence that varies as a function of latitude and season (Dirksen et al., 2011). Although NO₂ in the stratosphere is more zonally symmetric than in the troposphere, there is still spatial structure that is important for understanding the morphology of stratospheric NO₂, itself, while complicating the retrieval of tropospheric NO₂ from satellite-derived slant columns. The accuracy of the inferred tropospheric contribution critically depends on the characterization and separation of stratospheric NO₂. The procedure used to determine the two components of the NO₂ vertical column will be referred to as the stratosphere-troposphere separation (STS) algorithm.

Determining the relative amounts of stratospheric and tropospheric NO₂ from a given absorption spectrum is inherently difficult. Although the shape of the NO₂ absorption cross section varies with altitude (due to temperature), cross sections at different temperatures are not orthogonal. Therefore, the stratospheric and tropospheric NO₂ amounts cannot be independently determined from the spectral fit. Instead, most STS algorithms rely on spatial information from multiple slant columns measured over a wide geographic area. All such algorithms are prone to errors associated with the a priori information assumed about the stratospheric vertical column. The reference-sector (RS) method (Richter and Burrows, 2002; Van der A et al., 2008) assumes zonal invariance. The stratospheric vertical column at any latitude is set equal to the measured total column at the same latitude in the central Pacific Ocean. Because the central Pacific contains small background amounts of tropospheric NO₂, the RS method can slightly overestimate the stratospheric fraction of the column. Martin et al. (2002) corrected this by using model estimates of Pacific tropospheric NO₂. More importantly, the real stratospheric NO₂ varies with longitude, leading to potential inaccuracies in both the stratospheric and derived tropospheric vertical column. Other methods, such as

Applications to OMI

E. J. Bucsela et al.

Title Page

Abstract

Introduction

Conclusions

References

Tables

Figures



Back

Close

Full Screen / Esc

Printer-friendly Version

Interactive Discussion



Applications to OMI

E. J. Bucsela et al.

the image processing technique (IPT) of Leue et al. (2001) and Velders et al. (2001), and the wave-2 stratospheric model of Bucsela et al. (2006), allow for some longitudinal variation in stratospheric NO₂. However, like the RS method, the IPT and wave-2 algorithms required relatively simplistic assumptions about which regions to use in constructing the global NO₂ stratospheric field. The wave-2 model, in particular, can introduce stratospheric artifacts, especially at high latitudes (Dirksen et al., 2011). Some approaches have tried to capture more realistic structure in the stratospheric NO₂ field by using CTMs to estimate the spatial variation in stratospheric NO₂. In the Dutch OMI NO₂ (DOMINO) product (Boersma et al., 2011; Dirksen et al., 2011), OMI NO₂ measurements are assimilated in a CTM model. CTM-based algorithms require daily model runs and relatively complex assimilation schemes. As will be shown, CTM-based algorithms can also introduce occasional modeling artifacts. If independent stratospheric measurements are available, a more observation-based approach can be used. Beirle et al. (2010) and Hilboll et al. (2012) have described methods for combining nadir measurements from OMI or SCIAMACHY with limb measurements of stratospheric NO₂ from SCIAMACHY. Because the limb measurements are sparsely sampled, these approaches require significant spatial interpolation to obtain a continuous stratospheric field.

In this paper, we describe a new algorithm for the retrieval of NO₂ vertical columns using only nadir-viewing satellite slant-column measurements and simple climatologies. The algorithm is now used to produce NASA's Version 2 OMI NO₂ (OMNO2) Standard Product (SP2) and could be employed for other satellite measurements. For OMI data, SP2 is a significant improvement over the original SP1, which was based on the wave-2 STS algorithm. SP2 continues the philosophy of minimizing the use of model information in retrievals, but includes a number of features not present in SP1. The SP2 stratospheric slant column is estimated from the total slant column using an a priori monthly tropospheric NO₂ model climatology, but only where tropospheric contamination of the observed NO₂ column is small. The SP2 algorithm features improved air-mass factors based on new radiative transfer calculations and terrain reflectivities

Title Page	
Abstract	Introduction
Conclusions	References
Tables	Figures
◀	▶
◀	▶
Back	Close
Full Screen / Esc	
Printer-friendly Version	
Interactive Discussion	



Applications to OMI

E. J. Bucsela et al.

Title Page

Abstract

Introduction

Conclusions

References

Tables

Figures

◀

▶

◀

▶

Back

Close

Full Screen / Esc

Printer-friendly Version

Interactive Discussion



and uses monthly, rather than annual-mean NO_2 profile shapes. Cloud properties are obtained from the OMI OMCLDO2 data product, which was recently improved. We describe the algorithm in Sect. 2, explain error analysis in Sect. 3, and discuss additional considerations and comparisons with other datasets in Sect. 4. Section 5 contains a summary and conclusions.

2 Algorithm description

The architecture of the algorithm is summarized in the flow diagram in Fig. 1. Spectral data are fitted to obtain raw NO_2 slant columns, S' (Sect. 2.1), and are corrected for instrumental artifacts (also referred to as striping; see Sect. 2.3) to yield the de-striped slant columns, S . The data are analyzed to separate stratospheric and tropospheric NO_2 partial vertical columns, V_{strat} and V_{trop} , and to obtain total column amounts, V_{total} (Sect. 2.4). The stratospheric and tropospheric air mass factors, A_{strat} and A_{trop} (Sect. 2.2), used in the calculations are based on a priori information from radiative transfer (RT) and CTM models. The RT calculations used to process the OMI data in this study were carried out using TOMRAD (Dave, 1965). Additional details of the algorithm are given below.

2.1 OMI spectral fitting

The NO_2 slant columns used in this study were extracted from OMI spectra. The OMI instrument is a UV-VIS hyper-spectral, push-broom, nadir-viewing satellite spectrometer (Levelt et al., 2006) on the NASA EOS Aura satellite (Schoeberl et al., 2006), launched in July 2004. Aura has an equator crossing time of 13:30 LST and an orbital period of 99 min so that OMI views the entire sunlit portion of the Earth in 14.5 orbits. On each orbit, OMI makes simultaneous measurements in a swath of width 2600 km, divided into 60 fields of view (FOVs), or pixels. One swath is measured every two seconds, for approximately 1650 swaths from southern to northern terminator on the sunlit

Applications to OMI

E. J. Bucsela et al.

Title Page

Abstract

Introduction

Conclusions

References

Tables

Figures

◀

▶

◀

▶

Back

Close

Full Screen / Esc

Printer-friendly Version

Interactive Discussion



side of the earth. Swaths in adjacent orbits are nearly contiguous at the equator and overlap elsewhere. LST differences from the west to east sides of a swath range from approximately 1.5 h at the equator to several hours at mid- to high latitudes.

The NO_2 slant columns are estimated by spectral fitting of OMI earthshine radiances. The fitting algorithm uses the Differential Optical Absorption Spectroscopy (DOAS) method (Platt and Stutz, 2006), applied in the spectral range 405 nm to 465 nm (Boersma et al., 2002; Bucsela et al., 2006). The earthshine radiances are normalized by a reference OMI-measured solar irradiance spectrum [$R(\lambda) = I(\lambda)/F(\lambda)$]. The use of a static measured solar reference spectrum reduced much of the calibration-induced striping that was discovered soon after OMI operations began (Dobber et al., 2008). (The removal of residual striping is described in Sect. 2.3). The normalized spectra, $R(\lambda)$, are fitted to laboratory-measured trace gas absorption spectra at a fixed stratospheric temperature ($T_0 = 220$ K), a reference ring spectrum (Chance and Spurr, 1997), and a polynomial function that models the spectrally slowly varying scattering by clouds and aerosols and reflection by the Earth's surface. In the current version, the only trace gas absorption spectra considered are those of NO_2 (Vandaele et al., 1998), O_3 (Burrows et al., 1999), and H_2O (Harder and Brault, 1997). The temperature dependence of the NO_2 cross section is accounted for later in the algorithm. The trace gas absorption spectra used were produced by convolving high-resolution, laboratory-measured absorption spectra with the measured OMI slit function. The result of the spectral fit is the raw slant column density for each OMI pixel.

The calibrations of the 60 cross-track FOVs have relative biases that are observed to be persistent on time scales of several orbits to several days. As a result, the retrieved NO_2 slant columns show a pattern of stripes running along each orbital track. This instrumental artifact can be corrected to some extent using the “de-striping” procedure described in Sect. 2.3. A more severe effect is the “row anomaly” (RA), which was first noticed in the data in June 2007, and is likely caused by an obstruction in part of OMI's aperture. The extent of the RA has increased since 2007 and currently affects approximately half of the FOVs. Current RA information is available at

<http://www.knmi.nl/omi/research/product/rowanomaly-background.php>. Users of OMI data are discouraged from using FOVs flagged as RA-affected.

2.2 Air mass factors

In DOAS retrievals, the air mass factor, A , is the ratio of a slant column, S , to the vertical column, V , we want to retrieve. We write this relationship generically as $A = S/V$. The air mass factor is assumed to be wavelength-independent across the slant-column fitting window. In a given partial atmospheric region (stratosphere or troposphere), the air mass factor is computed as the ratio of the sum over layers of the slant sub-columns S_i to the sum of vertical sub-columns V_i :

$$A = \frac{S}{V} = \frac{\sum_i S_i}{\sum_i V_i} \quad (1)$$

where i is the layer index. The summation combines all layers in the appropriate partial atmospheric column. Temperature is assumed to be constant within a layer. Slant and vertical sub-columns can be represented as integrals over all pressures p within layer i :

$$S_i = \kappa \int_i dp \zeta(p) m(p) \alpha(p) \quad (2)$$

$$V_i = \kappa \int_i dp \zeta(p) \quad (3)$$

Here, $m(p)$ is the atmospheric scattering weight (also referred to as the “box” or “layer” air mass factor); $\alpha(p)$ is a temperature-correction factor for the NO_2 absorption cross section; $\zeta(p)$ is the a priori NO_2 mixing ratio, and κ is a constant equal to the reciprocal of the weight of an air molecule. The formulation in Eqs. (2) and (3) implicitly decouples atmospheric scattering and NO_2 absorption, as described by Palmer et al. (2001), so

Title Page

Abstract

Introduction

Conclusions

References

Tables

Figures

⏪

⏩

◀

▶

Back

Close

Full Screen / Esc

Printer-friendly Version

Interactive Discussion



that the $m(\rho)$ are independent of NO_2 amount. The temperature factor $\alpha(\rho)$ is needed to correct for the fixed-temperature NO_2 cross section ($T_0 = 220 \text{ K}$) used in the slant-column fitting and can be written as a function of the layer temperature T_i as

$$\alpha(\rho) = 1 - 0.003 [T(\rho) - T_0] \quad (4)$$

The coefficient 0.003 (units K^{-1}) was obtained empirically by fitting synthetic radiance spectra with NO_2 cross sections measured at several temperatures. This coefficient is in line with temperature correction coefficients proposed in Boersma et al. (2002, 2004).

For partly cloudy scenes, we use an independent-pixel approximation for the air mass factor (e.g., Martin et al., 2002) and express scattering weights as the weighted sum of cloudy and clear components, $m(\rho)^{\text{cloudy}}$, and $m(\rho)^{\text{clear}}$, respectively:

$$m(\rho) = w m(\rho)^{\text{cloudy}} + (1 - w) m(\rho)^{\text{clear}} \quad (5)$$

Here the weighting factor, w , denotes cloud/aerosol radiance fraction (CRF), the fraction of the measured radiation that comes from clouds and aerosols. In the SP1 and SP2 algorithms, aerosols are not distinguished from clouds, since weakly absorbing aerosols can have similar effects on the air mass factor in some circumstances (Boersma et al., 2011). The value of w is generally larger than the $\text{O}_2\text{-O}_2$ geometrical cloud fraction at 470 nm since the clouds are assumed to be optically thick with an effective Lambertian albedo of 0.8 (Stammes et al., 2008). The cloudy and clear scattering weights for a given observation depend on parameters including viewing geometry, surface (terrain or cloud) pressure, and surface reflectivity. Scattering weights are computed and stored a priori in six-dimensional look-up tables (LUT) generated from a radiative transfer model. For clear-sky scattering weights, the six LUT parameters are solar zenith angle (SZA), viewing zenith angle (VZA), relative azimuth angle (RAA), terrain reflectivity (R_t), terrain pressure (P_t), and atmospheric pressure level, (ρ). For cloudy scattering weights, we treat clouds as opaque Lambertian surfaces and

Applications to OMI

E. J. Bucsela et al.

Title Page

Abstract

Introduction

Conclusions

References

Tables

Figures

◀

▶

◀

▶

Back

Close

Full Screen / Esc

Printer-friendly Version

Interactive Discussion



Applications to OMI

E. J. Bucsela et al.

replace the terrain reflectivity and terrain pressure with cloud reflectivity ($R_c = 0.8$) and cloud optical centroid pressure (P_c), respectively. The latter is estimated with the OMI O_2-O_2 cloud algorithm (Acaretta et al., 2004; Snee et al., 2008).

The SP2 scattering weights are computed from parameter sets that have been improved relative to SP1. In particular, the terrain reflectivities, which were derived from GOME (Koelemeijer et al., 2003) in SP1 are now based on OMI measurements (Kleipool et al., 2008). Terrain pressures are obtained as described by Boersma et al. (2011) from a 3 km digital elevation model provided with the Aura data. The reflectivities and other parameters are no longer assumed to vary linearly between tabulated values, as was the case in SP1, and are now interpolated using Lagrange polynomials. The resolution in the six-dimensional parameter space has also been increased. In the new algorithm, the number of nodal points in SZA, VZA, RAA, R_t , P_t , and ρ are 9, 6, 5, 8, 6, and 35, respectively. These improvements reduce interpolation errors noted in SP1 (Dirksen et al., 2011) by up to 15 %.

The a priori NO_2 mixing ratio profiles for the air mass factor calculations in SP2 are obtained from the GMI CTM (Duncan et al., 2007; Strahan et al., 2007). The model simulates the stratosphere and troposphere and includes emissions, aerosol microphysics, chemistry, deposition, radiation, advection, and other important chemical and physical processes, such as lightning NO_x production (Duncan et al., 2007). The GMI chemical mechanism combines the stratospheric mechanism described by Douglass et al. (2004) with a detailed tropospheric O_3-NO_x -hydrocarbon chemistry originating from the Harvard GEOS-Chem model (Bey et al., 2001) and is driven by GEOS-5 meteorological fields at the resolution of 2° latitude \times 2.5° longitude (Rienecker et al., 2008). The vertical extent of the model is from the surface to 0.01 hPa, with 72 levels and a vertical resolution ranging from ~ 150 m in the boundary layer to ~ 1 km in the free troposphere and lower stratosphere. Model outputs were sampled at the LST of OMI overpass, and monthly mean profiles were derived using four years (2004–2007) of simulation. In contrast, SP1 used annual mean tropospheric profiles for 1997 from a GEOS-Chem simulation (Bey et al., 2001; Martin et al., 2002b), with only a single

Title Page

Abstract

Introduction

Conclusions

References

Tables

Figures

◀

▶

◀

▶

Back

Close

Full Screen / Esc

Printer-friendly Version

Interactive Discussion



profile used for the stratosphere (Bucsela et al., 2006). Unlike the stratospheric air mass factor, which depends mainly on the viewing geometry, the air mass factor in the troposphere is particularly sensitive to the NO₂ profile shape. Model profile shapes vary by geographic region and exhibit daily variability as well, as validated by in situ measurements (e.g., Boersma et al., 2008; Bucsela et al., 2008). Our sensitivity studies indicated that monthly mean profiles captured the seasonal variation sufficiently well so that daily profiles were not included in the SP2 algorithm.

2.3 De-stripped slant columns

As described in Sect. 2.1, an instrumental artifact introduces a bias in the retrieved OMI NO₂ slant columns, resulting in the appearance of orbital “stripes” when the data are mapped. The de-stripping algorithm computes the mean cross-track biases using raw NO₂ slant columns and stratospheric air mass factors from five consecutive orbits over clean regions (30° S to 5° N). This approach relies on identifying and estimating cross-track bias in slant columns from cross-track variation in the stratospheric air mass factors. An initial estimate of the bias δ_i for each cross-track position i is computed from the mean slant column $\{S'\}_i$ and stratospheric air mass factor $\{A_{\text{strat}}\}_i$ for that cross-track position and the average slant column $\{\{S'\}_i\}$ and average stratospheric air mass factor $\{\{A_{\text{strat}}\}_i\}$ over the entire swath from 30° S to 5° N. The computation of the entire swath averages excludes all scan positions that have extreme values of $\{S'\}_i/\{A_{\text{strat}}\}_i$ ($> 10^{17} \text{ cm}^{-2}$) and those known, a priori, to be affected by the row anomaly. The initial bias estimate is

$$\delta_i = \{S'\}_i - [\{A_{\text{strat}}\}_i \{\{S'\}_i\} / \{\{A_{\text{strat}}\}_i\}]. \quad (6)$$

The final value of the cross-track bias is re-computed from Eq. (6) by applying an additional screening criterion in the calculation of $\{\{S'\}_i\}$ and $\{\{A_{\text{strat}}\}_i\}$. The cross-track scan positions whose δ_i values lie outside a $\pm 2\sigma$ interval are excluded to ensure that very high or low values of the bias in any of the cross-track scan positions (including

[Title Page](#)
[Abstract](#)
[Introduction](#)
[Conclusions](#)
[References](#)
[Tables](#)
[Figures](#)
[◀](#)
[▶](#)
[◀](#)
[▶](#)
[Back](#)
[Close](#)
[Full Screen / Esc](#)
[Printer-friendly Version](#)
[Interactive Discussion](#)


those affected by the RA) do not affect the average. The resulting cross-track bias for a given OMI orbit is a set of 60 correction constants that vary about the mean. At each pixel in the orbit, the corresponding bias is subtracted from the measured slant column S' to give a corrected (“de-stripped”) slant column S .

5 2.4 Stratosphere-troposphere separation (STS)

The STS scheme described in this study takes advantage of the fact that, over most of the earth, the NO_2 absorption contributing to the slant column measurements is almost entirely stratospheric. Therefore, a simple and reasonable initial estimate of the stratospheric vertical column is the ratio of the de-stripped measured slant column to the (nearly geometric) stratospheric air mass factor:

$$V_{\text{init}} = S/A_{\text{strat}}. \quad (7)$$

In areas with relatively little tropospheric NO_2 , we obtain the value of the stratospheric vertical column by subtracting a fixed model estimate of the (small) tropospheric column from V_{init} and applying spatial smoothing to the resultant geographic field. Where there is substantial tropospheric NO_2 pollution, the stratosphere is estimated by spatial interpolation from the surrounding clean regions. The tropospheric vertical column is then computed as the difference between S and the stratospheric slant column, divided by tropospheric air mass factors.

Figure 2 illustrates the steps of the STS algorithm for one day of data, beginning with the spectrally fitted slant columns (Fig. 2a) and initial vertical columns V_{init} (Fig. 2b). The following seven steps summarize subsequent computations.

1. Subtract an a priori troposphere from V_{init} to get initial stratospheric vertical column.
2. Mask the field wherever tropospheric contamination exceeds a threshold.
3. Bin this initial stratospheric vertical-column estimate onto a geographic grid.

Title Page

Abstract

Introduction

Conclusions

References

Tables

Figures

⏪

⏩

◀

▶

Back

Close

Full Screen / Esc

Printer-friendly Version

Interactive Discussion



Applications to OMI

E. J. Bucsela et al.

4. Interpolate the binned vertical columns over masked areas.
5. Identify and eliminate “hot spots” in the stratospheric field.
6. Smooth and interpolate to pixel-center coordinates to give the final V_{strat} at each FOV.
7. Subtract the stratospheric contribution to get the tropospheric vertical column.

For steps 1 and 2, we first compute an a priori tropospheric slant column, S_{trop} , at each satellite pixel

$$S_{\text{trop}} = V_{\text{trop.a.priori}} A_{\text{trop}} \quad (8)$$

where $V_{\text{trop.a.priori}}$ is a geographically gridded, monthly mean model of NO_2 climatology of tropospheric vertical columns, and A_{trop} is the tropospheric air mass factor. The NO_2 climatology used in computing $V_{\text{trop.a.priori}}$ is the same as that used in the calculation of A_{trop} .

The initial estimate of the stratospheric field V_{strat}^0 (Fig. 2c) is computed as:

$$V_{\text{strat}}^0 = (S - S_{\text{trop}}) / A_{\text{strat}} \quad (9)$$

The algorithm then masks V_{strat}^0 for all pixels in which the tropospheric contamination of the NO_2 column is large. Masked pixels, shown as white areas in Fig. 2d, are eliminated from the stratospheric field calculation. The masking threshold is chosen to exclude pixels where V_{init} would exceed the actual stratospheric vertical column by more than a value ε . We require

$$(S_{\text{trop}} / A_{\text{strat}}) < \varepsilon \quad (10)$$

In the current algorithm, we chose an absolute threshold of $\varepsilon = 0.3 \times 10^{15} \text{ cm}^{-2}$ to limit the stratospheric vertical column uncertainty introduced by the a priori troposphere to a

Title Page

Abstract

Introduction

Conclusions

References

Tables

Figures

◀

▶

◀

▶

Back

Close

Full Screen / Esc

Printer-friendly Version

Interactive Discussion



Applications to OMI

E. J. Bucsela et al.

Title Page

Abstract

Introduction

Conclusions

References

Tables

Figures

◀

▶

◀

▶

Back

Close

Full Screen / Esc

Printer-friendly Version

Interactive Discussion



value of $0.2 \times 10^{15} \text{ cm}^{-2}$ or less. This uncertainty is consistent with previous estimates of uncertainty in the stratospheric NO_2 column (see Sect. 3.2) and is comparable to pixel noise associated with the slant column uncertainty (see Sect. 3). Using this masking scheme allows polluted pixels to remain unmasked where the lower troposphere is obscured by clouds. These unmasked pixels provide a more robust stratospheric retrieval in polluted areas than would be possible if all polluted regions were automatically masked. Conversely in regions where amounts of tropospheric NO_2 are relatively small ($\sim 0.5 \times 10^{15} \text{ cm}^{-2}$), tropospheric NO_2 can still contaminate the measurements if skies are clear and surface reflectivities are high. Examples are the Sahara and southern Arabian Peninsula, which require more masking than similarly unpolluted ocean regions (see Fig. 2d). We have chosen an absolute, rather than relative, threshold to assess tropospheric contamination of the observed column, since using a relative threshold leads to unnecessary masking of areas where the magnitude of small stratospheric columns begins to approach the absolute measurement uncertainty. Globally, the fraction of pixels masked is approximately constant throughout the year and ranges from about 10 % in the southern hemisphere to nearly 35 % in the Northern Hemisphere.

Steps 3–6 are performed with the stratospheric field data binned on a uniform $1^\circ \times 1^\circ$ geographic grid. A separate global stratospheric field is constructed for each orbit by forming weighted averages of the data in each $1^\circ \times 1^\circ$ bin and including data from the adjacent ± 7 orbits. Largest weights are assigned to data from the “target” orbit, so that adjacent orbits are essentially used only when data from the target orbit are unavailable. The weighting scheme minimizes the effects of mixing data from different local times in overlapping orbits with the data from the target orbit. Any unfilled bins are then interpolated using a 2-D averaging function in the form of a rectangular window of dimensions δ_{Lon} in longitude and δ_{Lat} degrees in latitude. At middle latitudes, we use a window of $\delta_{\text{Lon}} \sim 30^\circ$ and $\delta_{\text{Lat}} \sim 20^\circ$, but we modify these values at low and high latitudes. In particular, the longitude dimension near the equator is increased to 360 degrees to reduce synoptic-scale contamination of the stratospheric field by NO_2 enhancements due to tropical lightning. Martin et al. (2007) have discussed the existence

Applications to OMI

E. J. Bucsela et al.

Title Page

Abstract

Introduction

Conclusions

References

Tables

Figures

◀

▶

◀

▶

Back

Close

Full Screen / Esc

Printer-friendly Version

Interactive Discussion



of longitudinally broad tropospheric LNO₂ enhancements in the tropics between South America and Africa. The binned, interpolated field is shown in Fig. 2e. To further reduce contamination of the stratosphere by tropospheric NO₂ not accounted for in the climatology, we use statistical criteria to identify and mask tropospheric hot spots (step 5). For hot-spot removal, we employ a smaller averaging window of $\delta_{\text{Lon}} \sim 15^\circ$ and $\delta_{\text{Lat}} \sim 10^\circ$. The V_{strat} value in the bin at the center of the window is masked and replaced by the mean if its V_{strat} exceeds the mean by more than 1.5 standard deviations. A comparison of Fig. 2e and f shows the result of the hot-spot removal. Note the removal of small areas of locally enhanced NO₂ in western Canada, the eastern Gulf of Mexico, and in various locations throughout Asia. Finally, the stratospheric field is smoothed using a small window of $\delta_{\text{Lon}} \sim 5^\circ$ and $\delta_{\text{Lat}} \sim 3^\circ$ and interpolated from the $1^\circ \times 1^\circ$ grid back to the pixel-center coordinates. The smoothing step effectively degrades the spatial scale of resolvable stratospheric features to approximately 300 km so that any smaller-scale features in the V_{init} field will be interpreted as tropospheric.

The NO₂ tropospheric column at each pixel is the difference between the total and the stratospheric columns, computed as follows:

$$V_{\text{trop}} = (S - V_{\text{strat}}A_{\text{strat}})/A_{\text{trop}} \quad (11)$$

where S is the de-striped total measured slant column (Sect. 2.3) and A_{strat} and A_{trop} are the air mass factors (derived from a priori and cloud information as described in Sect. 2.2). Tropospheric values are generally positive, as seen in Fig. 2h, but local negative values may occur at any pixel where the binning, interpolation, and/or smoothing in the STS algorithm results in a V_{strat} value larger than V_{init} . The total column is the sum of the tropospheric and stratospheric columns:

$$V_{\text{total}} = V_{\text{strat}} + V_{\text{trop}} \quad (12)$$

Note that V_{total} is generally larger than V_{init} , since A_{trop} is typically smaller than A_{strat} , especially where tropospheric NO₂ is concentrated in the boundary layer and/or hidden by clouds.

3 Error estimates

The uncertainties in the total column amounts result from uncertainties in (1) the fitted NO₂ slant columns, (2) the stratospheric and tropospheric air mass factors, and (3) the algorithm used to separate the stratosphere and troposphere (STS). Descriptions of these errors in the context of OMI NO₂ retrievals may be found in Boersma et al. (2004, 2011) and Wenig et al. (2008). The uncertainties in the slant column amounts have been described previously (Boersma et al., 2004, 2011) and will not be discussed in detail here. For data collected during the first two to three years of the mission, the rms fitting error in the OMI NO₂ slant column had a median value of approximately 10¹⁵ cm⁻², which is on the order of 10% of the total slant column for polluted regions. For swath positions affected by the row anomaly (see Sect. 2.1), we calculate NO₂ values but do not estimate uncertainties. We treat the *S*, *A*, and STS errors as statistically independent and discuss the latter two in Sects. 3.1 and 3.2. The combined errors for the vertical column retrievals are given in Sect. 3.3.

3.1 Errors in air mass factors

The air mass factor (A_{strat} or A_{trop}) is computed as shown in Eqs. (1)–(5). A general expression for the air-mass-factor uncertainty, σ_A , can be written as a sum of variances:

$$(\sigma_A)^2 = (\sigma_A^m)^2 + (\sigma_A^{\text{CTM}})^2 \quad (13)$$

where σ_A^m is the net air-mass-factor error associated with the scattering weights, m , and σ_A^{CTM} is the net air-mass-factor error associated with the CTM used for the NO₂ profile shape. The parameters that most affect the scattering weights are the terrain reflectivity, R ; the cloud radiance fraction, w (w also implicitly accounts for aerosols (Boersma et al., 2011)); and the effective cloud pressure (also referred to as optical centroid pressure) P_c . The parameters relating to the CTM are the NO₂ sub-column

Title Page

Abstract

Introduction

Conclusions

References

Tables

Figures

◀

▶

◀

▶

Back

Close

Full Screen / Esc

Printer-friendly Version

Interactive Discussion



Applications to OMI

E. J. Bucsela et al.

Title Page

Abstract

Introduction

Conclusions

References

Tables

Figures

◀

▶

◀

▶

Back

Close

Full Screen / Esc

Printer-friendly Version

Interactive Discussion



profile, V_i , and temperature profile, T_i . In general, the uncertainties in these quantities are not independent; e.g., an overestimation of R can lead to an underestimation of w , and the derived cloud pressure P_c can also be related to w in cloud retrieval algorithms (Sneep et al., 2008). Likewise, the temperature profile T_i affects the model's prediction of NO_2 mixing ratios, $\zeta(p)$. Uncertainties in the viewing geometry and terrain pressure are neglected in this error formulation, although errors in the latter can affect integrated profile amounts, particularly over mountainous terrain (Schaub et al., 2007; Boersma et al., 2008; Hains et al., 2010; Russell et al., 2011).

In spite of these interdependencies, we assume, for computational convenience, that these parameters can be decoupled as follows:

$$(\sigma_A^m)^2 = (\sigma_A^R)^2 + (\sigma_A^w)^2 + (\sigma_A^{P_c})^2 \quad (14)$$

$$(\sigma_A^{\text{CTM}})^2 = (\sigma_A^\zeta)^2 + (\sigma_A^T)^2 \quad (15)$$

where σ_A^R , σ_A^w , and $\sigma_A^{P_c}$ are the air-mass-factor errors due to errors in terrain reflectivity, R , cloud radiance fraction, w , and cloud pressure, P_c , respectively. We also assume σ_A^ζ and σ_A^T are the respective air-mass-factor errors due to errors in the model NO_2 mixing-ratio profile, ζ_i , and temperature profile, T_i . Properly accounting for the actual interdependencies of the parameters decoupled in Eqs. (14) and (15) might reduce the overall errors. In that regard, the overall air-mass-factor uncertainties derived here can be treated as upper limits.

We compute the terms on the right-hand sides of Eqs. (14) and (15) from Eqs. (1)–(5) and from a priori estimates of the uncertainties σ_R , σ_w , σ_{P_c} , σ_ζ , and σ_T in terrain reflectivity, cloud-radiance fraction, cloud pressure, NO_2 profile, and temperature profile, respectively, and the sensitivities of A to each of these parameters. Using Eqs. (1)–(5), we can write simplified expressions for the variances $(\sigma_A^\beta)^2$ in the five parameters $\beta = R, w, P_c, \zeta$, or T . If the atmosphere is divided into N vertical layers ($i = 1, \dots, N$), we

define an N -element Jacobian column vector \mathbf{J}_β and its (row) transpose \mathbf{J}_β^T . Each element $(\mathbf{J}_\beta)_i$ is the derivative of A (Eq. 1) with respect to parameter β in layer i . With these definitions, the five variances can be written in compact matrix notation, with the corresponding explicit expressions for the Jacobian elements as follows:

$$(\sigma_A^R)^2 = \mathbf{J}_R^T (\mathbf{U} \sigma_R^2) \mathbf{J}_R \quad \text{where} \quad (\mathbf{J}_R)_i = \frac{(1-w)\kappa}{V} \int_i dp (\partial m^{\text{clear}} / \partial R) \alpha \zeta \quad (16)$$

$$(\sigma_A^W)^2 = \mathbf{J}_W^T (\mathbf{U} \sigma_W^2) \mathbf{J}_W \quad \text{where} \quad (\mathbf{J}_W)_i = \frac{\kappa}{V} \int_i dp (m^{\text{cloudy}} - m^{\text{clear}}) \alpha \zeta \quad (17)$$

$$(\sigma_A^{P_c})^2 = \mathbf{J}_{P_c}^T (\mathbf{U} \sigma_{P_c}^2) \mathbf{J}_{P_c} \quad \text{where} \quad (\mathbf{J}_{P_c})_i = \frac{\kappa}{V} \int_i dp (\partial m / \partial P_c) \alpha \zeta \quad (18)$$

$$(\sigma_A^\zeta)^2 = \mathbf{J}_\zeta^T \mathbf{S}_\zeta \mathbf{J}_\zeta \quad \text{where} \quad (\mathbf{J}_\zeta)_i = \frac{\kappa}{V} \int_i (dp m \alpha - A) \quad (19)$$

$$(\sigma_A^T)^2 = \mathbf{J}_T^T \mathbf{S}_T \mathbf{J}_T \quad \text{where} \quad (\mathbf{J}_T)_i = \frac{-0.003\kappa}{V} \int_i dp m \zeta \quad (20)$$

In Eqs. (16)–(20), \mathbf{U} is defined as an $N \times N$ -unit matrix (matrix of all elements equal to one). \mathbf{S}_ζ , and \mathbf{S}_T are the $N \times N$ -element covariance matrices for the a priori model NO_2 mixing-ratio and temperature profiles, respectively. In general, for parameter β , the (i, j) element of the covariance matrix is the expectation value of the product of the deviations $(\sigma_\beta)_i$ and $(\sigma_\beta)_j$ from their respective mean values, $(\mathbf{S}_\beta)_{i,j} = \langle (\sigma_\beta)_i (\sigma_\beta)_j \rangle$. The ζ and T covariance matrices can be estimated with daily profiles from the CTM, by considering the respective average covariances of ζ and T within each layer.

Combining Eqs. (13)–(20), we summarize the net variance in the air mass factor as

$$(\sigma_A)^2 = \mathbf{J}_R^T (\mathbf{U} \sigma_R^2) \mathbf{J}_R + \mathbf{J}_W^T (\mathbf{U} \sigma_W^2) \mathbf{J}_W + \mathbf{J}_{P_c}^T (\mathbf{U} \sigma_{P_c}^2) \mathbf{J}_{P_c} + \mathbf{J}_\zeta^T \mathbf{S}_\zeta \mathbf{J}_\zeta \quad (21)$$

In this expression, we have omitted the uncertainty due to temperature, since the error it introduces in the uncertainty relative to the other terms was found to be negligible.



Applications to OMI

E. J. Bucsela et al.

Title Page

Abstract

Introduction

Conclusions

References

Tables

Figures

◀

▶

◀

▶

Back

Close

Full Screen / Esc

Printer-friendly Version

Interactive Discussion



Equation (21) can be applied to both the stratospheric and tropospheric air mass factors. In practice, however, the A_{strat} is very nearly geometrical and has a very small uncertainty. For simplicity in calculation, we assume a fixed nominal 2% error in this value: $\sigma_{A_{\text{strat}}} = 0.02 A_{\text{strat}}$. Under clear skies (ignoring uncertainties related to clouds), the error in A_{trop} is a function of uncertainties in terrain reflectivity and the NO_2 profile shape. Assuming a nominal uncertainty in terrain reflectivity of $\sigma_R \sim 0.015$ (Wenig et al., 2008), the associated error A_{trop} is on the order of 10 to 15%, and a similar uncertainty results from errors in the profile (Bucsela et al., 2008). Therefore, a conservative estimate of clear-sky relative uncertainty in A_{trop} is 20%. When clouds are present, we compute uncertainties in A_{trop} of 30 to 80%.

3.2 Errors in the estimated stratosphere

The stratospheric vertical-column uncertainty, $\sigma_{V_{\text{strat}}}$, from the STS algorithm depends on a number of factors, including the conditions associated with the slant-column measurement, the STS algorithm parameters, and errors associated with the a priori tropospheric model. Measurement errors relate to the geographic region of the measurement, the local cloud parameters (cloud radiance fraction and cloud pressure), and the degree of tropospheric pollution affecting the region. Sources of retrieval-parameter error include the masking thresholds (for the initial masking and hot-spot removal) and the widths of the geographical averaging functions. Finally, the a priori tropospheric estimate introduces both random-type errors, due to differences between the monthly mean climatology and daily tropospheric profiles and any systematic errors affecting the model.

Because of the multiple dependencies, the stratospheric error is difficult to quantify. However, we can make a reasonable estimate by combining the effects of the three largest independent sources of uncertainty: (1) $\sigma_{S_{\text{trop}}^{\text{CTM}}}$ are errors in the a priori S_{trop} due to uncertainty in the CTM tropospheric vertical column, (2) $\sigma_{S_{\text{trop}}^{A_{\text{trop}}}}$ are a priori S_{trop} errors due to A_{trop} , and (3) $\sigma_{\delta V_{\text{strat}}}$ are stratospheric interpolation errors in the masked regions

(see Sect. 4.1.2). We write the combined variance as

$$(\sigma_{V_{\text{strat}}})^2 = (\sigma_{S_{\text{trop}}^{\text{CTM}}/A_{\text{strat}}})^2 + (\sigma_{S_{\text{trop}}^{A_{\text{trop}}}}/A_{\text{strat}})^2 + (\sigma_{\delta V_{\text{strat}}})^2 \quad (22)$$

We conservatively estimate the errors from sources (1) and (2) (first two terms) to be $\sim 50\%$. Therefore, by Eq. (10), with $\varepsilon = 0.3 \times 10^{15} \text{ cm}^{-2}$, these errors are $< 0.15 \times 10^{15} \text{ cm}^{-2}$ each. The third term in Eq. (22) applies only to masked areas (see Sect. 4.1.2). An estimate of its value was obtained from an analysis of simulated data. Using the monthly mean GMI model NO_2 profiles and daily views of geometry, pressure, reflectivity, and cloud parameters from OMI, a set of simulated slant-column measurements was constructed. The STS algorithm was then applied to these slant columns and the retrieved stratospheric vertical columns were compared to those of the original model. Histograms of the stratospheric errors in the masked regions for four months are shown in Fig. 3, which indicates $1\text{-}\sigma$ errors of approximately $0.1 \times 10^{15} \text{ cm}^{-2}$. Therefore, the combined stratospheric vertical-column error computed from Eq. (22) is on the order of $0.2 \times 10^{15} \text{ cm}^{-2}$. Errors in masked (polluted) regions can be slightly larger than this value, while errors in the cleanest areas (e.g., high-latitude, unpolluted areas) are typically significantly smaller. The use of $0.2 \times 10^{15} \text{ cm}^{-2}$ as an approximate value for stratospheric uncertainty is consistent with previous estimates by Boersma et al. (2004) and Bucsela et al. (2006). The masking threshold of $0.3 \times 10^{15} \text{ cm}^{-2}$ was chosen, in part, to make the total stratospheric vertical-column uncertainty close to this value. Section 4.1 offers further discussions of the effects of errors associated with the STS algorithm.

3.3 Vertical column errors

The uncertainties in the retrieved vertical-column amounts are calculated by treating the uncertainties in S , V_{strat} , A_{strat} , and A_{trop} as independent. Based on the definitions of tropospheric and total columns in (Eqs. 11 and 12), this assumption yields the following

variances in the tropospheric and total vertical columns:

$$\sigma_{V_{\text{trop}}}^2 = [\sigma_S^2 + (A_{\text{strat}}\sigma_{V_{\text{strat}}})^2 + (V_{\text{strat}}\sigma_{A_{\text{strat}}})^2 + (V_{\text{trop}}\sigma_{A_{\text{trop}}})^2]/A_{\text{trop}}^2 \quad (23)$$

$$\sigma_V^2 = \sigma_{V_{\text{trop}}}^2 + \sigma_{V_{\text{strat}}}^2 (1 - 2A_{\text{strat}}/A_{\text{trop}}) \quad (24)$$

5 where σ_S , $\sigma_{V_{\text{strat}}}$, $\sigma_{A_{\text{strat}}}$, and $\sigma_{A_{\text{trop}}}$ are the uncertainties in S , V_{strat} , A_{strat} , A_{trop} , described in Sects. 3 through 3.2. Global mean tropospheric vertical-column errors are typically on the order of 1×10^{15} for clear skies and $> 3 \times 10^{15} \text{ cm}^{-2}$ as the cloud radiance frac-
10 tion approaches unity. The tropospheric errors are driven mainly by the slant-column uncertainty when pollution is low and by both slant-column and air-mass-factor uncertainties under polluted conditions. Relative tropospheric vertical column uncertainties in cloudy, polluted regions can approach 100%.

4 Discussion and comparisons with other data sets

The main components that distinguish the SP2 algorithm from SP1 and other satellite NO_2 retrieval schemes involve the STS and tropospheric air mass factors. In this sec-
15 tion, we further examine the STS algorithm, compare with OMI retrievals from other algorithms, and re-examine validation using in situ measurements.

4.1 Retrieval effects of a priori assumptions in the STS algorithm

The a priori tropospheric NO_2 columns and the masking, interpolation, and smoothing components of the STS algorithm affect NO_2 retrieval accuracy. In general, over the
20 cleanest areas (open-ocean and high-latitude regions), the SP2 algorithm yields V_{strat} values that are approximately as accurate as the NO_2 slant columns and contain only small amounts of a priori model information from the tropospheric climatology. Relatively little independent tropospheric information is retrieved from these regions, but



Applications to OMI

E. J. Bucsela et al.

Title Page

Abstract

Introduction

Conclusions

References

Tables

Figures

◀

▶

◀

▶

Back

Close

Full Screen / Esc

Printer-friendly Version

Interactive Discussion



local enhancements relative to the a priori troposphere can be observed. Over polluted (masked) regions, the SP2 algorithm provides V_{trop} retrievals that are largely independent of the local a priori tropospheric column amounts, although these retrievals do depend on the assumed local profile shapes via the air mass factors.

To examine these assertions more closely, consider idealized, noise-free retrievals over unmasked and masked regions (see steps 2 and 5 in Sect. 2.4). We assume that the “true” stratospheric air mass factor, $\overline{A_{\text{strat}}}$, is equal to its a priori estimate, A_{strat} , and is invariant on scales smaller than the widths of the smoothing windows: $\langle A_{\text{strat}} \rangle \approx A_{\text{strat}}$ (on this scale we ignore the effects of viewing geometry). In this discussion, we use an underline for variables to represent “true” (as opposed to a priori) atmospheric values, brackets $\langle \rangle$ to indicate window averages, and a prime (') to designate values in masked (polluted) areas.

4.1.1 Retrievals in unmasked (clean) regions

If the measured slant column is the sum of the true stratospheric and tropospheric slant columns, $S = \overline{S_{\text{strat}}} + \overline{S_{\text{trop}}}$, then it can be shown from Eq. (9) that the retrieved stratospheric vertical column in unmasked (clean) regions is given by

$$V_{\text{strat_RET}} = \overline{\langle V_{\text{strat}} \rangle} - (\langle S_{\text{trop}} \rangle - \overline{\langle S_{\text{trop}} \rangle}) / A_{\text{strat}} \quad (25)$$

where $\langle V_{\text{strat}} \rangle$ is the window-averaged true stratospheric vertical column. Equation (25) states that the retrieved stratospheric vertical column is the average of the true stratospheric vertical column plus an error term from the difference between the true and a priori tropospheric slant columns. When the a priori tropospheric slant column is correct and the true stratospheric field is smooth on the scale of the smoothing window, then the stratospheric retrieval is unbiased: $V_{\text{strat_RET}} \approx \overline{V_{\text{strat}}}$.

If the true stratospheric field is homogeneous within the averaging window, then from Eq. (11), the retrieved troposphere in the unmasked regions is

$$V_{\text{trop_RET}} = \overline{V_{\text{trop}}} (\overline{A_{\text{trop}}} / A_{\text{trop}}) + (\langle S_{\text{trop}} \rangle - \overline{\langle S_{\text{trop}} \rangle}) / A_{\text{trop}} \quad (26)$$

Furthermore, when the a priori tropospheric air mass factors are accurate ($A_{\text{trop}} \approx \overline{A_{\text{trop}}}$) and slowly varying, Eq. (26) becomes

$$V_{\text{trop_RET}} \approx \langle V_{\text{trop}} \rangle + (\overline{V_{\text{trop}}} - \langle V_{\text{trop}} \rangle) \quad (27)$$

Equation (27) shows that, in unmasked regions, the *retrieved* tropospheric vertical column is approximately equal to the a priori mean value (first term). However, the retrieval has additional fine-scale structure equal to the difference between the true tropospheric vertical column and its mean (second term).

4.1.2 Retrievals in masked (polluted) regions

The retrieved stratospheric vertical column in masked areas, $V'_{\text{strat_RET}}$, is actually the interpolation-window average of the retrieved stratosphere in surrounding unmasked and masked regions. We assume the “true” stratosphere in masked areas as the similarly averaged true stratosphere from surrounding regions, plus an amount, δV_{strat} , which varies from point to point inside the mask. The standard deviation of δV_{strat} is $\sigma_{\delta V_{\text{strat}}}$, which was derived in Sect. 3.2 from the histogram widths in Fig. 3. With these definitions, the tropospheric retrieval in a masked region can be shown to be

$$V'_{\text{trop_RET}} = \overline{V'_{\text{trop}} (A'_{\text{trop}} / A'_{\text{trop}})} + (\langle S_{\text{trop}} \rangle - \overline{\langle S_{\text{trop}} \rangle}) / A'_{\text{trop}} + \delta V_{\text{strat}} (A'_{\text{strat}} / A'_{\text{trop}}) \quad (28)$$

where A'_{strat} and A'_{trop} are the a priori stratospheric and tropospheric air mass factors in the masked area, and $\overline{A'_{\text{trop}}}$ is the true tropospheric air mass factor. As before, $\langle S_{\text{trop}} \rangle$ and $\overline{\langle S_{\text{trop}} \rangle}$ are the smoothed a priori and true tropospheric slant columns, respectively, in the surrounding unmasked areas. We want our retrieval $V'_{\text{trop_RET}}$ to be as close as possible to the true troposphere $\overline{V'_{\text{trop}}}$, and the three terms in Eq. (28) identify three possible sources of error. The first arises from potential mismatch of the true and a priori tropospheric air mass factors, $\overline{A'_{\text{trop}}}$ and A'_{trop} . The true tropospheric

Title Page

Abstract

Introduction

Conclusions

References

Tables

Figures

⏪

⏩

◀

▶

Back

Close

Full Screen / Esc

Printer-friendly Version

Interactive Discussion



Applications to OMI

E. J. Bucsela et al.

Title Page

Abstract

Introduction

Conclusions

References

Tables

Figures

◀

▶

◀

▶

Back

Close

Full Screen / Esc

Printer-friendly Version

Interactive Discussion



vertical column will be scaled by their ratio. The second term shows errors due to the incorrect estimation of the a priori tropospheric slant columns in the surrounding areas. The third term describes tropospheric errors resulting from differences between the true stratosphere in the masked region and the mean stratosphere estimated from the surrounding regions. The second and third terms increase as the tropospheric air mass factor in the masked region (the denominator of each) decreases due to increasing aerosol or cloud fraction, for example. The result is that any biases caused by non-zero values for δV_{strat} or for $\langle S_{\text{trop}} \rangle - \overline{\langle S_{\text{trop}} \rangle}$ outside the mask will be amplified as the cloud fraction for a given pixel inside the mask increases. The bias is bounded, because measurements with large cloud fractions generally switch to the unmasked case described in Sect. 4.1.1.

4.1.3 Examples using simulated data

Figure 4 shows retrievals of simulated OMI slant-column data. The plots represent nadir pixels along sections of two OMI orbits, with viewing geometry and cloud parameters taken from the orbital data. In this simulation, we assume that all a priori air mass factors are correct, i.e., the true air mass factors are the same as those used in the retrieval. Figure 4a and c illustrates respective stratospheric and tropospheric retrievals in an unmasked (clean) part of the eastern Pacific. The retrieved stratospheric vertical column (red curve in Fig. 4a) is biased high because the simulated tropospheric data were intentionally made 50 % larger than the a priori troposphere in the unmasked regions. This bias affects the retrieved stratosphere via the second term in Eq. (25). Figure 4c shows the corresponding tropospheric retrieval. As expected from Eq. (27), the retrieval (red) follows the a priori (blue) rather than the true data (black), on average. However, it is evident that some of the smaller-scale differential structure in the original data is preserved in the retrieval.

Retrievals in a masked region of the eastern US are shown in Fig. 4b and d. The differences between the true and retrieved stratospheres (Fig. 4c) are similar to the unmasked case (Fig. 4a), except that some regional variability is apparent. These

Applications to OMI

E. J. Bucsela et al.

Title Page

Abstract

Introduction

Conclusions

References

Tables

Figures

◀

▶

◀

▶

Back

Close

Full Screen / Esc

Printer-friendly Version

Interactive Discussion



deviations are due to intentional non-zero values of δV_{strat} used in constructing the stratospheric NO_2 field. An example can be seen for latitudes 30°N – 37°N , where the stratospheric retrieval (interpolation from surrounding unmasked regions) underestimates the stratospheric data. The corresponding troposphere in the masked region is shown in Fig. 4d. Unlike the unmasked case, the retrieved troposphere here (red) is mostly independent of the a priori troposphere (blue) and is generally a good estimate of the true data (black). An obvious exception around 30°N – 37°N latitude results from the previously noted stratospheric underestimation, which leads to a tropospheric overestimation. Elsewhere, the tropospheric vertical column is slightly underestimated by an absolute amount comparable to that of the unmasked troposphere (Fig. 4c). As in the unmasked case, this underestimation is due to the error in the a priori troposphere for the clean regions. The relative effect in this case appears small, since overall tropospheric columns are much larger in the masked region (note the difference in y-axis scaling for Fig. 4c and d).

In summary, the absolute stratospheric retrieval errors are generally small in most areas. The magnitude of the error depends on the magnitude of the bias between the a priori and true tropospheric fields. For OMI, we estimate that this bias introduces a stratospheric uncertainty of $\sim 0.2 \times 10^{15} \text{ cm}^{-2}$ or $< 10\%$. When tropospheric air mass factors are accurate, our simulations show that the absolute tropospheric vertical-column errors due to stratospheric errors are also small (on the order of $0.5 \times 10^{15} \text{ cm}^{-2}$) in both masked and unmasked regions. The corresponding relative tropospheric errors in unmasked regions may be large due to the small tropospheric background amounts in those regions. Errors in tropospheric air mass factors will lead to proportional increases in both the absolute and relative tropospheric vertical-column errors in all areas.

4.1.4 Masking and interpolation sensitivity tests

The retrieved stratospheric field was examined for sensitivity to parameters that control the initial masking and interpolation in the STS algorithm. These steps are illustrated

Applications to OMI

E. J. Bucsela et al.

Title Page

Abstract

Introduction

Conclusions

References

Tables

Figures

◀

▶

◀

▶

Back

Close

Full Screen / Esc

Printer-friendly Version

Interactive Discussion



in Fig. 2d and e. We modified the masking threshold and the dimensions of the interpolation function (window) and computed the resultant stratospheric fields. In each case, the field based on the nominal parameters (see Sect. 2.4) was subtracted from the modified field. The results, shown in Fig. 5, suggest that the retrieval is fairly robust with respect to the threshold and window dimensions. In Fig. 5a, the masking threshold was reduced from its nominal value of $0.3 \times 10^{15} \text{ cm}^{-2}$ to $0.2 \times 10^{15} \text{ cm}^{-2}$, and in Fig. 5b, the threshold was increased to $0.4 \times 10^{15} \text{ cm}^{-2}$. The reduced threshold increases the number of masked pixels by a factor of ~ 2 , while the threshold increase approximately halves the masked-pixel count. The difference in the resultant V_{strat} is generally smaller than $0.5 \times 10^{15} \text{ cm}^{-2}$ and is less than $0.1 \times 10^{15} \text{ cm}^{-2}$ over most of the earth. The biggest effects are seen for the smaller threshold ($0.2 \times 10^{15} \text{ cm}^{-2}$), since this threshold would result in more than half of northern-hemisphere pixels being masked, leaving little data from which to accurately interpolate the stratospheric field. Tests involving the interpolation algorithm are shown in Fig. 5c and d. In these figures, the latitude and longitude dimensions of the window were approximately halved and doubled, respectively. Results show that effects on the stratospheric field are even smaller than those seen in the threshold tests. We have also found that changing the shape of the interpolation function (e.g., from boxes to circles) makes a negligible difference in the resultant stratosphere.

4.2 Comparisons with other NO_2 retrieval algorithms and models

Using NO_2 slant columns from one day of OMI data for illustration, we compare SP2 retrievals with those from the SP1 algorithm (Bucsela et al., 2006) and the DOMINO v2 algorithm (Boersma et al., 2011). The retrieved stratospheric fields for one day are shown in Fig. 6, along with the GMI model field for the same date. The GMI stratosphere was sampled at the OMI overpass time and adjusted by empirical scaling factors to give approximate agreement in magnitude with the retrieved OMI stratosphere over the Pacific. For simplicity, the scaling factors were taken to be linear functions of latitude only and to vary between about 1.1 and 1.4. A comparison of Fig. 6b and d

Applications to OMI

E. J. Bucsela et al.

Title Page

Abstract

Introduction

Conclusions

References

Tables

Figures

◀

▶

◀

▶

Back

Close

Full Screen / Esc

Printer-friendly Version

Interactive Discussion



shows that synoptic-scale structures in the model stratosphere are qualitatively similar to those retrieved by the SP2 algorithm. The stratosphere of the SP1 retrieval lacks structure on this scale and contains artifacts associated with the wave-2 assumption in the SP1 retrieval. Examples are the low SP1 stratospheric NO_2 values in western Asia and the band of enhanced NO_2 across the southern US and parts of the Atlantic Ocean and North Sea. In some of these regions, the SP1 stratospheric values exceed the values of V_{init} (Fig. 2b), which should not occur, apart from measurement noise, since tropospheric NO_2 amounts must be positive. Such artifacts are also evident in the v2 DOMINO stratospheric field over the North Atlantic, parts of Siberia, and at southern high latitudes. DOMINO also shows stronger cross-track diurnal variation in comparison to SP2 and V_{init} (Fig. 2b). Tropospheric retrievals for the same day in March are shown in Fig. 7. The tropospheric fields for all three OMI products (Fig. 7a, b, and c) are qualitatively similar to the GMI March monthly mean field shown in Fig. 4.4d. The SP1 field shown in Fig. 7a has been re-computed using an off-line version of the SP1 algorithm that retains any negative values of tropospheric NO_2 . The SP2 tropospheric retrieval shows relatively few instances of negative tropospheric NO_2 compared to the other two OMI products. Monthly means from January and July (not shown) indicate that approximately 8 to 9 % of V_{trop} columns retrieved from SP2 are significantly negative, defined here as $V_{\text{trop}} < -0.2 \times 10^{15} \text{ cm}^{-2}$. DOMINO tropospheric vertical columns have a somewhat higher frequency of negative values, but these occur predominantly in regions that are cloudy or snow-covered (and thus flagged as unreliable). Approximately 21 % of the mostly cloudy (cloud radiance fraction > 0.5) V_{trop} retrievals from DOMINO are significantly negative, compared to ~ 15 % of DOMINO retrievals in relatively cloud-free regions. A comparison of Figs. 6c and 7c shows that some of the negative tropospheric values in DOMINO are associated with the strong cross-track variation in the DOMINO stratospheric field.

Larger-scale similarities and differences in the NO_2 retrievals can be seen by examining monthly means. Figure 8 compares monthly zonal means of stratospheric NO_2 in January and July from SP1, SP2 and DOMINO, and the longitudinal variation of

monthly mean tropospheric NO₂ in northern mid-latitudes for the same two months. In January and July, the stratospheric zonal means (Fig. 8a and b) are similar in all three products, with the SP2 slightly higher and the SP1 slightly lower than DOMINO. Larger differences are evident in the tropospheric means shown in Fig. 8c and d. Although the mean values of SP2 and DOMINO are similar (DOMINO is slightly lower in January and slightly higher in July at most longitudes), SP1 is consistently higher than SP2 by almost a factor of two in July. This discrepancy is likely due to the tropospheric air mass factors used in the SP1 retrieval, which did not account for the seasonal variability in NO₂ profile shape (Lamsal et al., 2010).

4.3 Comparison with in situ measurements from INTEX-B

Validation of the OMNO2 SP2 is the subject of ongoing studies (Lamsal et al., 2013). Preliminary results suggest improved agreement with independent datasets for SP2 relative to SP1. The following example shows how NO₂ from SP2 compares with data from the Intercontinental Chemical Transport Experiment (INTEX-B).

The INTEX-B campaign was conducted from March to May 2006 and included in situ data from the airborne Laser-Induced Fluorescence (LIF) instrument (Thornton et al., 2000, 2003), which measured NO₂ mixing ratios with an estimated accuracy of ± 10 % or ± 5 ppt. Mixing-ratio profiles were obtained at a number of locations in and near the Gulf of Mexico and parts of the Pacific Ocean. The former region included land measurements at polluted locations near Mexico City and Houston.

The LIF data were analyzed and compared by Bucsela et al. (2008), Boersma et al. (2008), and Hains et al. (2010) with OMI data. In the present study, we have employed a similar approach to that of Bucsela et al. (2008). LIF data were selected for analysis based on the cloud/aerosol amount, altitude range of the aircraft, and temporal (< 3 h) and spatial (< 20 km) proximity to the OMI overpass data. The profiles were integrated for comparison with OMI NO₂ tropospheric columns. All profiles required extrapolation in altitude, both above and below the actual measurements, to cover the full tropospheric column, and the amount of extrapolation was accounted for in the

Title Page

Abstract

Introduction

Conclusions

References

Tables

Figures

⏪

⏩

◀

▶

Back

Close

Full Screen / Esc

Printer-friendly Version

Interactive Discussion



uncertainties assigned to each profile. Comparisons with OMI were made using x - and y -error weighted linear regression.

The following information describes our analysis of three different sets of OMNO2 data. The data are from (1) SP1 applied to collection 2 OMI data (as in the original study of Bucselá et al., 2008), (2) SP1 applied to collection 3, and (3) SP2 applied to collection 3. The collection 2 slant columns were retrieved from the OMI spectra based on pre-launch calibrations. Improved post-launch calibrations were used to construct a collection 3 data set in 2007, as described by Dobber et al. (2008). All OMI examples shown previously in this study are based on collection 3 data. A summary of the comparison results is shown in Fig. 9. In general, the agreement between the LIF and OMI data is good in all cases. Figure 9a shows that the SP1 algorithm, using the original collection 2 OMI slant columns yields vertical columns slightly below those of the in situ LIF columns (see also Bucselá et al., 2008). The regression OMI vs. in situ yields slope = 0.9, y -intercept = $0.1 \times 10^{15} \text{ cm}^{-2}$, and Pearson's correlation coefficient $r = 0.83$. Using the collection 3 spectral radiances and the same SP1 algorithm (Fig. 9b), we obtain slope = 1.2, y -intercept = $0.2 \times 10^{15} \text{ cm}^{-2}$, and $r = 0.72$, respectively. This result implies a modest overestimate of NO_2 by OMI relative to the in situ measurements. Figure 9c shows the re-analysis of the same collection 3 data using the new SP2 algorithm. In this case, the slope and intercept are approximately unity and zero, respectively, and the correlation coefficient is $r = 0.76$. The slope and intercept in the latest OMNO2 dataset indicate the best agreement with the INTEX-B data of the three comparison figures. Although this analysis was based on springtime rather than summertime data, the smaller tropospheric columns in SP2 relative to SP1 (for the same collection 3 dataset) appear consistent with Fig. 8d and the results of Lamsal et al. (2013).

Applications to OMI

E. J. Bucselá et al.

Title Page

Abstract

Introduction

Conclusions

References

Tables

Figures



Back

Close

Full Screen / Esc

Printer-friendly Version

Interactive Discussion



5 Summary and conclusions

The retrieval algorithm described in this paper represents an improvement on many previous and existing methods for retrieving NO₂ vertical columns from nadir-viewing satellites. SP2 provides a more realistic, detailed stratosphere and troposphere and has a relatively small dependence on a priori information and assumptions. In the stratospheric retrieval, there is no assumption of global zonal invariance as in reference-sector methods, no assumption of wave-2 zonal variation as in SP1, no use of ancillary stratospheric limb measurements (e.g., Beirle et al., 2010), and no stratospheric CTM scaling or assimilation as employed in the OMI DOMINO product. The stratosphere computed in SP2 requires a monthly tropospheric climatology, but this is applied only to clean or cloudy regions where the errors associated with the climatology are comparable to nominal measurement uncertainties in the stratosphere. In other regions, the stratosphere is interpolated with the introduction of small additional errors in the stratospheric field. The effect on the retrieved stratosphere of modest changes in the interpolation parameters (e.g., the extent of masking or the interpolation-window size and shape) is relatively small.

Tests using simulated data show reasonable accuracy in the SP2 retrievals. Recent validation studies comparing OMNO2 SP2 with independent measurements also suggest improvement over SP1-based validations. We note fewer instances of negative tropospheric vertical columns relative to SP1 and the KNMI DOMINO product. However, the general agreement between OMNO2 and DOMINO has improved with the introduction of the SP2 algorithm. This agreement is noteworthy, given the very different STS algorithms used in the two products. The discrepancies between polluted summertime tropospheric vertical columns from OMI and those from independent measurements have been greatly reduced in SP2 compared to SP1 and are also small relative to DOMINO.

The quality of the SP2 data is currently being established by independent measurements in ongoing validation campaigns from ground, aircraft, and satellite instruments.

Title Page

Abstract

Introduction

Conclusions

References

Tables

Figures

⏪

⏩

◀

▶

Back

Close

Full Screen / Esc

Printer-friendly Version

Interactive Discussion



Applications to OMI

E. J. Bucsela et al.

Title Page

Abstract

Introduction

Conclusions

References

Tables

Figures

◀

▶

◀

▶

Back

Close

Full Screen / Esc

Printer-friendly Version

Interactive Discussion



Better error estimates in the SP2 product should facilitate the comparisons, and future work will help to refine the error estimates. Differences in the behavior of the SP2 algorithm under clear/cloudy, polluted/clean, and masked/unmasked conditions should also be kept in mind when comparing OMI datasets. Versions of the SP2 algorithm are also

5 planned for testing with data from other satellite instruments including SCIAMACHY, GOME-2 and TROPOMI.

Acknowledgement. The authors wish to thank the editor and referees for their helpful comments in preparing this paper. We acknowledge the NASA Earth Science Division for funding of the OMI Standard NO₂ product development and analysis. The Dutch-Finnish-built OMI instrument is part of the NASA EOS Aura satellite payload. The OMI instrument is managed by

10 KNMI and The Netherlands Agency for Aerospace Programs (NIVR).

References

Acarreta, J. R., deHaan, J. F., and Stammes, P.: Cloud pressure retrieval using the O₂-O₂ absorption band at 477 nm, *J. Geophys. Res.*, 109, D05204, doi:10.1029/2003JD003915, 2004.

15

Beirle, S., Platt, U., von Glasow, R., Wenig, M., and Wagner, T.: Estimate of nitrogen oxide emissions from shipping by satellite remote sensing, *Geophys. Res. Lett.*, 31, L18102, doi:10.1029/2004GL020312, 2004.

Beirle, S., Kühl, S., Pukite, J., and Wagner, T.: Retrieval of tropospheric column densities of NO₂ from combined SCIAMACHY nadir/limb measurements, *Atmos. Meas. Tech.*, 3, 283–299, doi:10.5194/amt-3-283-2010, 2010.

20

Beirle, S., Boersma, K. F., Platt, U., Lawrence, M. G., and Wagner, T.: Megacity Emissions and Lifetimes of Nitrogen Oxides Probed from Space, *Science*, 333, 1737–1739, 2011.

Bey, I., Jacob, D. J., Yantosca, R. M., Logan, J. A., Field, B. D., Fiore, A. M., Li, Q., Liu, H., Mickley, L. J., and Schultz, M. G.: Global modeling of tropospheric chemistry with assimilated meteorology: Model description and evaluation, *J. Geophys. Res.*, 106, 23073–23095, 2001.

25

Boersma, K. F., Bucsela, E. J., Brinksma, E. J., and Gleason, J. F.: NO₂, in: OMI Algorithm Theoretical Basis Document, Vol. 4, OMI Trace Gas Algorithms, ATB-OMI-04, Version 2.0, 20,

Applications to OMI

E. J. Bucsela et al.

Title Page

Abstract

Introduction

Conclusions

References

Tables

Figures

◀

▶

◀

▶

Back

Close

Full Screen / Esc

Printer-friendly Version

Interactive Discussion



edited by: Chance, K., 13–36, NASA Distrib. Active Archive Cent., Greenbelt, Md., August, 2002.

Boersma, K. F., Eskes, H. J., and Brinksma, E. J.: Error analysis for tropospheric NO₂ from space, *J. Geophys. Res.*, 109, D04311, doi:10.1029/2003JD003962, 2004.

Boersma, K. F., Eskes, H. J., Veefkind, J. P., Brinksma, E. J., van der A, R. J., Sneep, M., van den Oord, G. H. J., Levelt, P. F., Stammes, P., Gleason, J. F., and Bucsela, E. J.: Near-real time retrieval of tropospheric NO₂ from OMI, *Atmos. Chem. Phys.*, 7, 2103–2118, doi:10.5194/acp-7-2103-2007, 2007.

Boersma, K. F., Jacob, D. J., Bucsela, E. J., Perring, A. E., Dirksen, R., van der A, R. J., Yantosca, R. M., Park, R. J., Wenig, M. O., Bertram, T. H., and Cohen, R. C.: Validation of OMI tropospheric NO₂ observations during INTEX-B and application to constrain NO_x emissions over the eastern United States and Mexico, *Atmos. Environ.*, 42, 4480–4497, doi:10.1016/j.atmosenv.2008.02.004, 2008.

Boersma, K. F., Eskes, H. J., Dirksen, R. J., van der A, R. J., Veefkind, J. P., Stammes, P., Huijnen, V., Kleipool, Q. L., Sneep, M., Claas, J., Leitão, J., Richter, A., Zhou, Y., and Brunner, D.: An improved tropospheric NO₂ column retrieval algorithm for the Ozone Monitoring Instrument, *Atmos. Meas. Tech. Discuss.*, 4, 2329–2388, doi:10.5194/amtd-4-2329-2011, 2011.

Bovensmann, H., Burrows, J. P., Buchwitz, M., Frerick, J., Noel, S., Chance, K. V., and Goede, A. P. H.: SCIAMACHY: Mission objectives and measurement modes, *J. Atmos. Sci.*, 56, 127–150, 1999.

Brewer, A. W., McElroy, C. T., and Kerr, J. B.: Nitrogen dioxide concentrations in the atmosphere, *Nature*, 246, 129, doi:10.1038/246129a0, 1973.

Bucsela, E. J., Celarier, E. A., Wenig, M. O., Gleason, J. F., Veefkind, J. P., Boersma, K. F., and Brinksma, E. J.: Algorithm for NO₂ vertical column retrieval from the Ozone Monitoring Instrument, *IEEE T. Geosci. Remote Sens.*, 44, 1245–1258, 2006.

Bucsela, E. J., Perring, A. E., Cohen, R. C., Boersma, K. F., Celarier, E. A., Gleason, J. F., Wenig, M. O., Bertram, T. H., Wooldridge, P. J., Dirksen, R., and Veefkind, J. P.: Comparison of tropospheric NO₂ from in situ aircraft measurements with near-real-time and standard product data from OMI, *J. Geophys. Res.*, 113, D16S31, doi:10.1029/2007JD008838, 2008.

Burrows, J. P., Richter, A., Dehn, A., Deters, B., Himmelmann, S., Voigt, S., and Orphal, J.: Atmospheric remote sensing reference data from GOME – 2. Temperature-dependent absorption cross-sections of O₃ in the 231–794 nm range, *J. Quant. Spectrosc. Ra.*, 61, 509–517, 1999a.

Applications to OMI

E. J. Bucsela et al.

Title Page

Abstract

Introduction

Conclusions

References

Tables

Figures

◀

▶

◀

▶

Back

Close

Full Screen / Esc

Printer-friendly Version

Interactive Discussion



- Burrows, J. P., Weber, M., Buchwitz, M., Rosanov, V. V., Ladstatter, A., Weissenmayer, A., Richter, A., DeBeek, R., Hoogen, R., Bramstedt, K., and Eichmann, K. U.: The Global Ozone Monitoring Experiment (GOME): Mission concept and first scientific results, *J. Atmos. Sci.*, 56, 151–175, 1999b.
- 5 Callies, J., Corpaccioli, E., Eisinger, M., Hahne, A., and Lefebvre, A.: GOME-2 – Metop’s Second Generation Sensor for Operational Ozone Monitoring, *ESA Bulletin*, 102, 28–36, 2000.
- Castellanos, P. and Boersma, K. F.: Reductions in nitrogen oxides over Europe driven by environmental policy and economic recession: *Scientific Reports*, 2, doi:10.1038/srep00265, 2012.
- 10 Chance, K. V. and Spurr, R. J. D.: Ring effect studies: Rayleigh scattering, including molecular parameters for rotational Raman scattering, and the Fraunhofer spectrum, *Appl. Opt.*, 36, 5224, doi:10.1364/AO.36.005224, 1997.
- Choi, Y., Wang, Y., Zeng, T., Cunnold, D., Yang, E.-S., Martin, R. V., Chance, K., Thouret, V., and Edgerton, E.: Springtime transitions of NO₂, CO, and O₃ over North America: model
- 15 evaluation and analysis, *J. Geophys. Res.*, 113, D20311, doi:10.1029/2007JD009632, 2008.
- Dave, J. V.: Multiple scattering in a non-homogeneous, Rayleigh atmosphere, *J. Atmos. Sci.*, 22, 273–279, 1965.
- Dirksen, R. J., Boersma, K. F., Eskes, H. J., Ionov, D. V., Bucsela, E. J., Levelt, P. F., and Kelder, H. M.: Evaluation of stratospheric NO₂ retrieved from the Ozone Monitoring Instrument: Intercomparison, diurnal cycle, and trending, *J. Geophys. Res.*, 116, D08305, doi:10.1029/2010JD014943, 2011.
- 20 Dobber, M. R., Kleipool, Q., Dirksen, R., Levelt, P. F., Jaross, G., Taylor, S., Kelly, T., Flynn, L., Leppelmeier, G., and Rozemeijer, N.: Validation of Ozone Monitoring Instrument level-1b data products, *J. Geophys. Res.*, 113, D15S06, doi:10.1029/2007JD008665, 2008.
- 25 Douglass A. R., Stolarski, R. S., Strahan, S. E., and Connell, P. S.: Radicals and reservoirs in the GMI chemistry and transport model: Comparison to measurements, *J. Geophys. Res.*, 109, D16302, doi:10.1029/2004JD004632, 2004.
- Duncan, B. N., Strahan, S. E., Yoshida, Y., Steenrod, S. D., and Livesey, N.: Model study of the cross-tropopause transport of biomass burning pollution, *Atmos. Chem. Phys.*, 7, 3713–3736, doi:10.5194/acp-7-3713-2007, 2007.
- 30 Frost, G. J., McKeen, S. A., Trainer, M., Ryerson, T. B., Neuman, J. A., Roberts, J. M., Swanson, A., Holloway, J. S., Sueper, D. T., Fortin, T., Parrish, D. D., Fehsenfeld, F. C., Flocke, F., Peckham, S. E., Grell, G. A., Kowal, D., Cartwright, J., Auerbach, N., and Habermann, T.:

Applications to OMI

E. J. Bucsela et al.

Effects of changing power plant NO_x emissions on ozone in the eastern United States: Proof of concept, *J. Geophys. Res.*, 111, D12306, doi:10.1029/2005JD006354, 2006.

Hains, J. C., Boersma, K. F., Kroon, M., Dirksen, R. J., Cohen, R. C., Perring, A. E., Bucsela, E. J., Volten, H., Swart, D. P. J., Richter, A., Wittrock, F., Schoenhardt, A., Wagner, T., Ibrahim, O. W., Van Roozendaal, M., Pinardi, G., Gleason, J. F., Veefkind, J. P., and Levelt, P. F.: Testing and improving OMI DOMINO tropospheric NO₂ using observations from the DANDELIONS and INTEX-B validation campaigns, *J. Geophys. Res.*, 115, D05301, doi:10.1029/2009JD012399, 2010.

Harder, J. W. and Brault, J. W.: Atmospheric measurements of water vapor in the 442-nm region, *J. Geophys. Res.*, 102, 6245–6252, doi:10.1029/96JD01730, 1997.

Hilboll, A., Richter, A., Rozanov, A., Hodnebrog, Ø., Heckel, A., Solberg, S., Stordal, F., and Burrows, J. P.: Retrieval of tropospheric NO₂ columns from SCIAMACHY combining measurements from limb and nadir geometries, *Atmos. Meas. Tech. Discuss.*, 5, 5043–5105, doi:10.5194/amtd-5-5043-2012, 2012.

Jaegle, L., Steinberger, L., Martin, R. V., and Chance, K.: Global partitioning of NO_x sources using satellite observations: Relative roles of fossil fuel combustion, biomass burning and soil emissions, *Faraday Discuss.*, 130, 407–423, doi:10.1039/b502128f, 2005.

Kim, S.-W., Heckel, A., McKeen, S. A., Frost, G. J., Hsie, E.-Y., Trainer, M. K., Richter, A., Burrows, J. P., Peckham, S. E., and Grell, G. A.: Satellite-observed U.S. power plant NO_x emission reductions and their impact on air quality, *Geophys. Res. Lett.*, 33, L22812, doi:10.1029/2006GL027749, 2006.

Kleipool, Q. L., Dobber, M. R., de Haan, J. F., and Levelt, P. F.: Earth surface reflectance climatology from 3 years of OMI data, *J. Geophys. Res.*, 113, D18308, doi:10.1029/2008JD010290, 2008.

Koelemeijer, R. B. A., De Haan, J. F., and Stammes, P.: A database of spectral surface reflectivity in the range 335 – 772 nm derived from 5.5 years of GOME observations, *J. Geophys. Res.*, 108, D24070, doi:10.1029/2002JD002429, 2003.

Lamsal, L. N., Martin, R. V., van Donkelaar, A., Celarier, E. A., Bucsela, E. J., Boersma, K. F., Dirksen, R., Luo, C., and Wang, Y.: Indirect validation of tropospheric nitrogen dioxide retrieved from the OMI satellite instrument: Insight into the seasonal variation of nitrogen oxides at northern midlatitudes, *J. Geophys. Res.*, 115, D05302, doi:10.1029/2009JD013351, 2010.

Title Page

Abstract

Introduction

Conclusions

References

Tables

Figures

◀

▶

◀

▶

Back

Close

Full Screen / Esc

Printer-friendly Version

Interactive Discussion



Applications to OMI

E. J. Bucsela et al.

Title Page

Abstract

Introduction

Conclusions

References

Tables

Figures

◀

▶

◀

▶

Back

Close

Full Screen / Esc

Printer-friendly Version

Interactive Discussion



- Lamsal, L. N.: Evaluation of improved operational standard tropospheric NO₂ retrievals from Ozone Monitoring Instrument using in situ and surface-based NO₂ observations, in preparation, 2013.
- Leue, C., Wenig, M., Wagner, T., Klimm, O., Platt, U., and Jähne, B.: Quantitative analysis of NO_x emissions from Global Ozone Monitoring Experiment satellite image suences, *J. Geophys. Res.* 106, 5493–5505, 2001.
- Levelt, P. F., Hilsenrath, E., Leppelmeier, G. W., van den Oord, G. B. J., Bhartia, P. K., Tamminen, J., de Haan, J. F., and Veefkind, J. P.: Science Objectives of the Ozone Monitoring Instrument, *IEEE Trans Geosci. Remote Sens.*, 44, 1199–1208, doi:10.1109/TGRS.2006.872333, 2006.
- Lin, J.-T., McElroy, M. B., and Boersma, K. F.: Constraint of anthropogenic NO_x emissions in China from different sectors: a new methodology using multiple satellite retrievals, *Atmos. Chem. Phys.*, 10, 63–78, doi:10.5194/acp-10-63-2010, 2010.
- Martin, R. V., Chance, K., Jacob, D. J., Kurosu, T. P., Spurr, R. J. D., Bucsela, E., Gleason, J., Palmer, P. I., Bey, I., Fiore, A. M., Li, Q., Yantosca, R. M., and Koelmeijer, R. B. A.: An improved retrieval of tropospheric nitrogen dioxide from GOME, *J. Geophys. Res.*, 107, 4437, doi:10.1029/2001JD001027, 2002a.
- Martin, R. V., Jacob, D. J., Logan, J. A., Bey, I., Yantosca, R. M., Staudt, A. C., Li, Q., Fiore, A. M., Duncan, B. N., Liu, H., Ginoux, P., and Thouret, V.: Interpretation of TOMS observations of tropical tropospheric ozone with a global model and in situ observations, *J. Geophys. Res.*, 107, 4351, doi:10.1029/2001JD001480, 2002b.
- Martin, R. V., Jacob, D. J., Chance, K., Kurosu, T. P., Palmer, P. I., and Evans, M. J.: Global inventory of nitrogen oxide emissions constrained by space-based observations of NO₂ columns, *J. Geophys. Res.*, 108, 4537, doi:10.1029/2003JD003453, 2003.
- Martin, R. V., Sioris, C. E., Chance, K. V., Ryerson, T. B., Bertram, T. H., Woolridge, P. J., Cohen, R. C., Neuman, J. A., Swanson, A., and Flocke, F. M.: Evaluation of space-based constraints on nitrogen oxide emissions with regional aircraft measurements over and downwind of eastern North America, *J. Geophys. Res.*, 111, D15308, doi:10.1029/2005JD006680, 2006.
- Martin, R. V., Sauvage, B., Folkins, I., Sioris, C. E., Boone, C., Bernath, P., and Ziemke, J.: Space-based constraints on the production of nitric oxide by lightning, *J. Geophys. Res.*, 112, D09309, doi:10.1029/2006JD007831, 2007.
- Noxon, J. F.: Nitrogen dioxide in the stratosphere and troposphere measured by ground-based absorption spectroscopy, *Science*, 189, 547–549, 1975.

Applications to OMI

E. J. Bucsela et al.

Title Page

Abstract

Introduction

Conclusions

References

Tables

Figures

◀

▶

◀

▶

Back

Close

Full Screen / Esc

Printer-friendly Version

Interactive Discussion



Palmer, P. I., Jacob, D. J., Chance, K., Martin, R. V., Spurr, R. J. D., Kurosu, T. P., Bey, I., Yantosca, R., and Fiore, A.: Air mass factor formulation for spectroscopic measurements from satellites: Application to formaldehyde retrievals from the Global Ozone Monitoring Experiment, *J. Geophys. Res.*, 106, 14539–14550, doi:10.1029/2000JD900772, 2001.

5 Platt, U.: Differential optical absorption spectroscopy (DOAS), in: *Air Monitoring by Spectrometric Techniques*, edited by: Sigrist, M. W., Vol. 127 of Chemical Analysis Series, 27–84, John Wiley, New York, 1994.

Platt, U. and Perner, D.: Measurements of atmospheric trace gases by long path differential UV/visible absorption spectroscopy, in: *Optical and Laser Remote Sensing*, edited by: Killinger, D. A. and Mooradian, A., 95–105, Springer Verlag, New York, 1983.

10 Platt, U. and Stutz, J.: *Differential Optical Absorption Spectroscopy (DOAS), Principle and Applications*, Springer Verlag Heidelberg, ISBN 3-340-21193-4, 2006.

Richter, A. and Burrows, J. P.: Tropospheric NO₂ from GOME measurements, *Adv. Space Res.*, 29, 1673–1683, doi:10.1016/S0273-1177(02)00100-X, 2002.

15 Richter, A., Burrows, J. P., Nüß, H., Granier, C., and Niemeier, U.: Increase in tropospheric nitrogen dioxide over China observed from space, *Nature*, 437, 129–132, 2005.

Russell, A. R., Valin, L. C., Bucsela, E. J., Wenig, M. O., and Cohen, R. C.: Space-based Constraints on Spatial and Temporal Patterns of NO_x Emissions in California, 2005–2008, *Environ. Sci. Technol.*, 44, 3608–3615, doi:10.1021/es903451j, 2010.

20 Russell, A. R., Perring, A. E., Valin, L. C., Bucsela, E. J., Browne, E. C., Wooldridge, P. J., and Cohen, R. C.: A high spatial resolution retrieval of NO₂ column densities from OMI: method and evaluation, *Atmos. Chem. Phys.*, 11, 8543–8554, doi:10.5194/acp-11-8543-2011, 2011.

Schaub, D., Brunner, D., Boersma, K. F., Keller, J., Folini, D., Buchmann, B., Berresheim, H., and Staehelin, J.: SCIAMACHY tropospheric NO₂ over Switzerland: estimates of NO_x lifetimes and impact of the complex Alpine topography on the retrieval, *Atmos. Chem. Phys.*, 7, 5971–5987, doi:10.5194/acp-7-5971-2007, 2007.

25 Schoeberl, M. R., Douglass, A. R., Hlsenrath, E., Bhartia, P. K., Beer, R., Waters, J. W., Gunson, M., Froidevaux, L., Gille, J., Barnett, J., Levelt, P. F., and Decola, P.: Overview of the EOS Aura Mission, *IEEE T. Geosci. Remote Sens.*, 44, 1066–1074, 2006.

30 Schumann, U. and Huntrieser, H.: The global lightning-induced nitrogen oxides source, *Atmos. Chem. Phys.*, 7, 3823–3907, doi:10.5194/acp-7-3823-2007, 2007.

Applications to OMI

E. J. Bucsela et al.

Title Page

Abstract

Introduction

Conclusions

References

Tables

Figures

◀

▶

◀

▶

Back

Close

Full Screen / Esc

Printer-friendly Version

Interactive Discussion



- Sneep, M., De Haan, J., Stammes, P., Wang, P., Vanbauce, C., Joiner, J., Vasilkov, A. P., and Levelt, P. F.: Three way comparison between OMI/Aura and POLDER/PARASOL cloud pressure products, *J. Geophys. Res.*, 113, D15S23, doi:10.1029/2007JD008694, 2008.
- Solomon, S. and Garcia, R. R.: On the distribution of long-lived tracers and chlorine species in the middle atmosphere, *J. Geophys. Res.*, 89, 11633–11644, 1984.
- Stammes, P., Sneep, M., de Haan, J. F., Veefkind, J. P., Wang, P., and Levelt, P. F.: Effective cloud fractions from the Ozone Monitoring Instrument: Theoretical framework and validation, *J. Geophys. Res.*, 113, D16S38, doi:10.1029/2007JD008820, 2008.
- Strahan, S. E., Duncan, B. N., and Hoor, P.: Observationally derived transport diagnostics for the lowermost stratosphere and their application to the GMI chemistry and transport model, *Atmos. Chem. Phys.*, 7, 2435–2445, doi:10.5194/acp-7-2435-2007, 2007.
- Suarez, M. J., Rienecker, M. M., Todling, R., Bacmeister, J., Takacs, L., Liu, H. C., Gu, W., Sienkiewicz, M., Koster, R. D., Gelaro, R., Stajner, I., and Nielsen, J. E.: The GEOS-5 Data Assimilation System–Documentation of Versions 5.0.1, 5.1.0, and 5.2.0 Technical Report Series on Global Modeling and Data Assimilation, v. 27, 2008.
- Thornton, J. A., Wooldridge, P. J., and Cohen, R. C.: Atmospheric NO₂: In situ laser-induced fluorescence detection at parts per trillion mixing ratios, *Anal. Chem.*, 72, 528–539, 2000.
- Thornton, J. A., Wooldridge, P. J., Cohen, R. C., Williams, E. J., Hereid, D., Fehsenfeld, F. C., Stutz, J., and Alicke, B.: Comparisons of in situ and long path measurements of NO in urban plumes, *J. Geophys. Res.*, 108, 4496, doi:10.1029/2003JD003559, 2003.
- Tie, X., Zhang, R., Brasseur, G., and Lei, W.: Global: NO_x production by lightning, *J. Atmos. Chem.*, 43, 61–74, 2002.
- Valks, P. and Loyola, D.: Algorithm theoretical basis document for GOME-2 total column products of ozone, minor trace gases, and cloud properties, Technical Report, DLR/GOME-2/ATBD/01, Iss.1/C, available at: http://www.wdc.dlr.de/sensors/gome2/DLR_GOME-2_ATBD_1C, 2008.
- Valks, P., Pinardi, G., Richter, A., Lambert, J.-C., Hao, N., Loyola, D., Van Roozendael, M., and Emmadi, S.: Operational total and tropospheric NO₂ column retrieval for GOME-2, *Atmos. Meas. Tech.*, 4, 1491–1514, doi:10.5194/amt-4-1491-2011, 2011.
- van der A, R. J., Eskes, H. J., Boersma, K. F., van Noije, T. P. C., Van Roozendael, M., DeSmedt, I., Peters, D. H. M. U., and Meijer, E. W.: Trends, seasonal variability and dominant NO_x source derived from a ten year record of NO₂ measured from space, *J. Geophys. Res.*, 113, D04302, doi:10.1029/2007JD009021, 2008.

Applications to OMI

E. J. Bucsela et al.

Title Page

Abstract

Introduction

Conclusions

References

Tables

Figures

◀

▶

◀

▶

Back

Close

Full Screen / Esc

Printer-friendly Version

Interactive Discussion



- Vandaele, A. C., Hermans, C., Simon, P. C., Carleer, M., Colin, R., Fally, S., Mérienne, M. F., Jenouvrier, A., and Coquart, B.: Measurements of the NO₂ absorption cross-section from 42000 cm⁻¹ to 10000 cm⁻¹ (238–1000 nm) at 220 K and 294 K, *J. Quant. Spectrosc. Ra.*, 59, 171–184, 1998.
- 5 Velders, G. J. M., Granier, C., Portmann, R. W., Pfeilsticker, K., Wenig, M., Wagner, T., Platt, U., Richter, A., and Burrows, J. P.: Global tropospheric NO₂ column distributions: Comparing three-dimensional model calculations with GOME measurements, *J. Geophys. Res.*, 106, 12643–12660, 2001.
- 10 Wenig, M. O., Cede, A. M., Bucsela, E. J., Celarier, E. A., Boersma, K. F., Veeffkind, J. P., Brinksma, E. J., Gleason, J. F., and Herman, J. R.: Validation of OMI tropospheric NO₂ column densities using direct-sun mode Brewer measurements at NASA Goddard Space Flight Center, *J. Geophys. Res.*, 113, D16S45, doi:10.1029/2007JD008988, 2008.
- 15 Zhang, Q., Streets, D. G., He, K., Wang, Y., Richter, A., Burrows, J. P., Uno, I., Jang, C. J., Chen, D., Yao, Z., and Lei, Y.: NO_x emission trends for China, 1995–2004: The view from the ground and the view from space, *J. Geophys. Res.*, 112, D22306, doi:10.1029/2007jd008684, 2007.

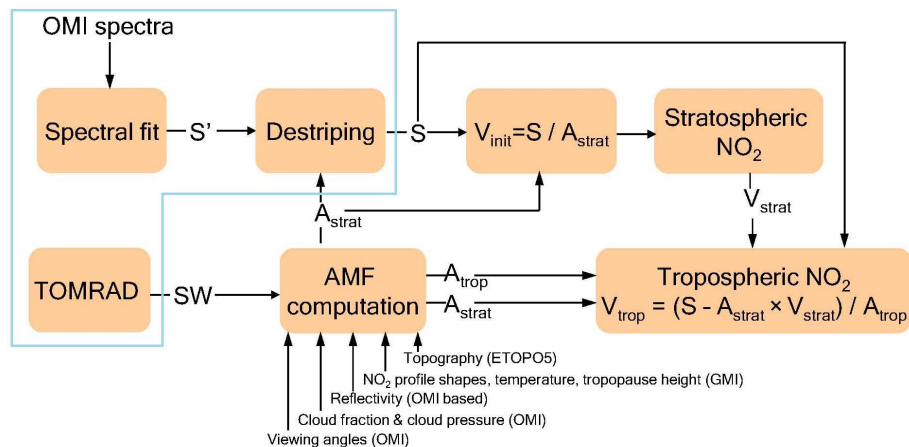


Fig. 1. Flow diagram of retrieval algorithm for stratospheric and tropospheric NO₂ columns. S , V , A , and SW represent slant column density, vertical column density, air mass factor, and scattering weight (m), respectively. The section outlined in blue is OMI-specific. TOMRAD is a forward vector radiative transfer model (Dave, 1965).

[Title Page](#)
[Abstract](#)
[Introduction](#)
[Conclusions](#)
[References](#)
[Tables](#)
[Figures](#)
[◀](#)
[▶](#)
[◀](#)
[▶](#)
[Back](#)
[Close](#)
[Full Screen / Esc](#)
[Printer-friendly Version](#)
[Interactive Discussion](#)

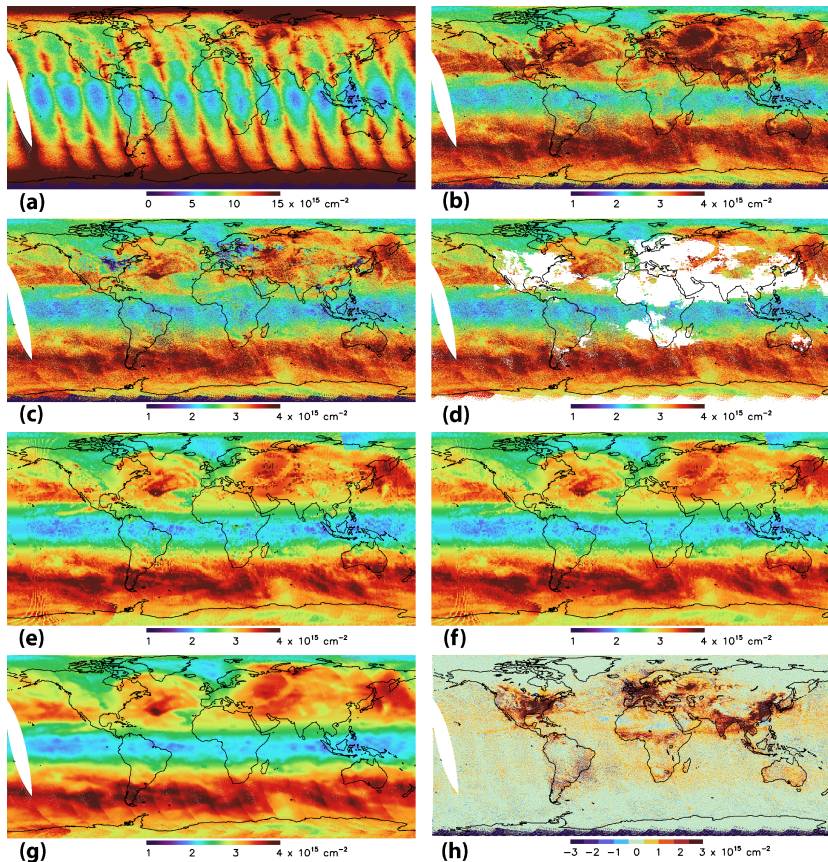



Fig. 2. Maps of 21 March 2005 OMI NO₂ data showing STS algorithm steps. **(a)** Slant columns. **(b)** V_{init} . **(c)** V_{init} minus a priori troposphere. **(d)** Same as **(c)**, but masked for pollution (white areas correspond to a masking threshold of $0.3 \times 10^{15} \text{ cm}^{-2}$). **(e)** Gridded, $V_{\text{strat}}^{\text{o}}$ with masked areas interpolated. **(f)** Hot-spots removed. **(g)** Stratosphere after final smooth, re-interpolated onto OMI pixel coordinates. **(h)** Tropospheric field.

Title Page

Abstract

Introduction

Conclusions

References

Tables

Figures

◀

▶

◀

▶

Back

Close

Full Screen / Esc

Printer-friendly Version

Interactive Discussion



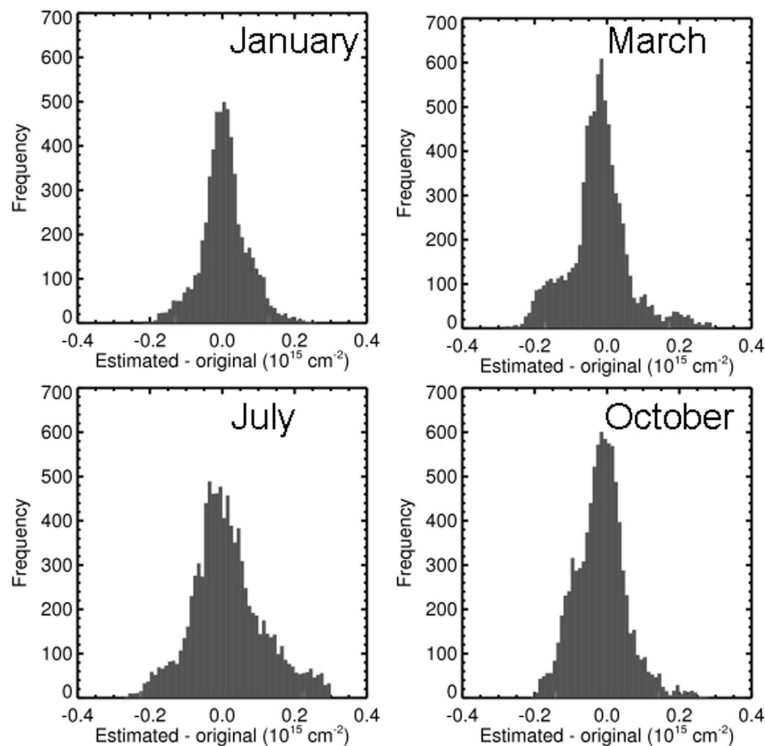


Fig. 3. Histograms of the difference between estimated and original stratospheric NO₂ columns over masked (polluted) areas based on simulated-data retrievals for January, March, July, and October 2005. Each histogram has a 2-sigma level deviation of approximately $0.2 \times 10^{15} \text{ cm}^{-2}$.

[Title Page](#)[Abstract](#)[Introduction](#)[Conclusions](#)[References](#)[Tables](#)[Figures](#)[◀](#)[▶](#)[◀](#)[▶](#)[Back](#)[Close](#)[Full Screen / Esc](#)[Printer-friendly Version](#)[Interactive Discussion](#)

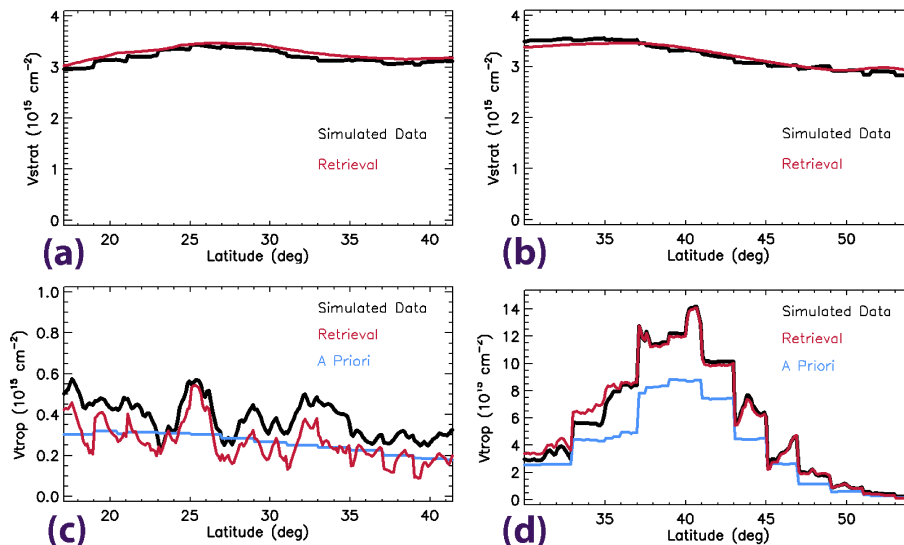


Fig. 4. NO₂ vertical column retrievals (red), using simulated data (black). The mean value of the tropospheric data (truth, black) was defined to be larger than that of the algorithm's a priori troposphere (blue). Shown are nadir pixels along two orbital segments: **(a)** and **(c)** are stratosphere and troposphere, respectively, for an unmasked segment in the eastern Pacific; **(b)** and **(d)** are stratosphere and troposphere, respectively, for a masked segment over eastern North America. In these simulations, geolocation, viewing geometry, and cloud parameters were taken from two orbits on 21 March 2005.

[Title Page](#)
[Abstract](#)
[Introduction](#)
[Conclusions](#)
[References](#)
[Tables](#)
[Figures](#)
[⏪](#)
[⏩](#)
[◀](#)
[▶](#)
[Back](#)
[Close](#)
[Full Screen / Esc](#)
[Printer-friendly Version](#)
[Interactive Discussion](#)

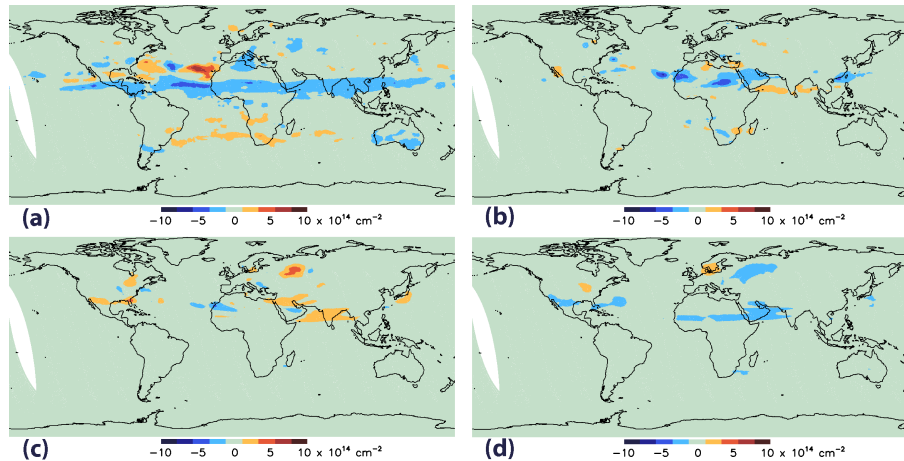



Fig. 5. Differences (= modified – nominal) in stratospheric field resulting from changes in masking threshold (nominal = $0.3 \times 10^{15} \text{ cm}^{-2}$) and interpolation window dimensions (see text) in the STS algorithm. **(a)** Tropospheric masking threshold decreased to $0.2 \times 10^{15} \text{ cm}^{-2}$. **(b)** Masking threshold increased to $0.4 \times 10^{15} \text{ cm}^{-2}$. **(c)** Interpolation window halved in latitude and longitude width relative to nominal size. **(d)** Interpolation window doubled in width.

[Title Page](#)
[Abstract](#)
[Introduction](#)
[Conclusions](#)
[References](#)
[Tables](#)
[Figures](#)
[⏪](#)
[⏩](#)
[◀](#)
[▶](#)
[Back](#)
[Close](#)
[Full Screen / Esc](#)
[Printer-friendly Version](#)
[Interactive Discussion](#)

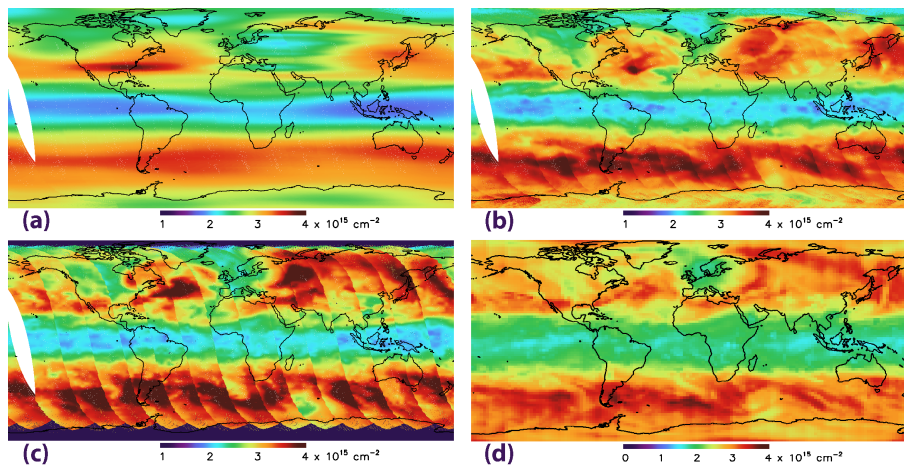



Fig. 6. Stratospheric NO_2 vertical column retrieval for the date 21 March 2005. **(a)** SP1. **(b)** SP2. **(c)** DOMINO. **(d)** GMI (scaled to the magnitude of SP2 using latitude-dependent scaling factors).

[Title Page](#)[Abstract](#)[Introduction](#)[Conclusions](#)[References](#)[Tables](#)[Figures](#)[◀](#)[▶](#)[◀](#)[▶](#)[Back](#)[Close](#)[Full Screen / Esc](#)[Printer-friendly Version](#)[Interactive Discussion](#)

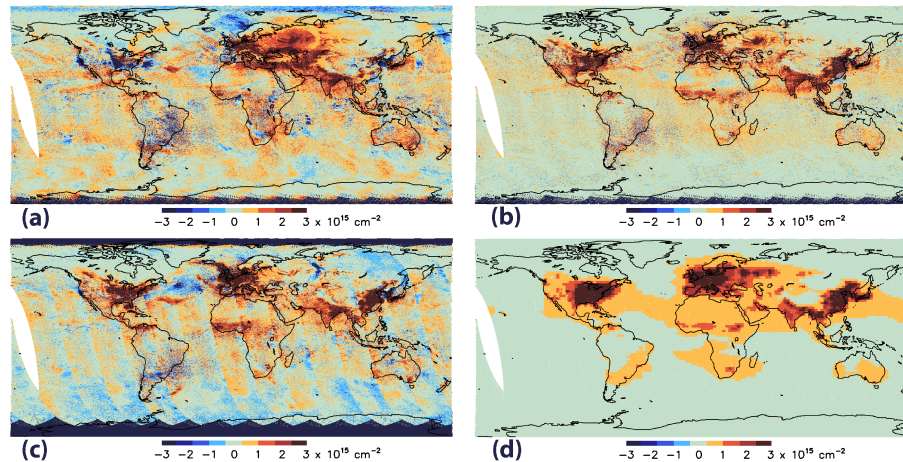


Fig. 7. Tropospheric NO₂ vertical column retrieval for the date 21 March 2005. **(a)** P1. **(b)** SP2. **(c)** DOMINO. **(d)** GMI. Note that all negative values in SP1 were set to zero in the original public product. Also note that most negative values in the DOMINO product occur in cloudy or snow-covered regions and are flagged as unreliable.

[Title Page](#)[Abstract](#)[Introduction](#)[Conclusions](#)[References](#)[Tables](#)[Figures](#)[◀](#)[▶](#)[◀](#)[▶](#)[Back](#)[Close](#)[Full Screen / Esc](#)[Printer-friendly Version](#)[Interactive Discussion](#)

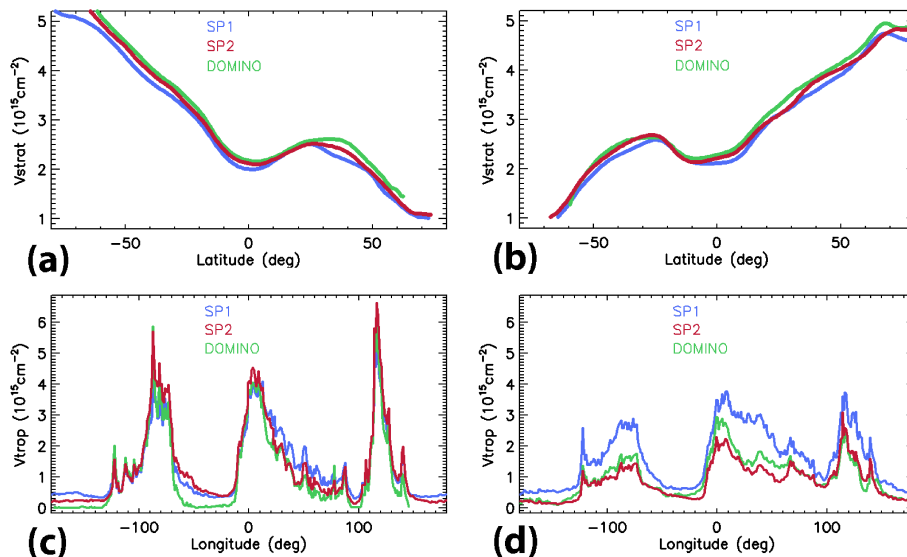


Fig. 8. Monthly mean NO₂ comparisons of SP1 (blue), SP2 (red), and DOMINO (green): **(a)** January stratospheric zonal mean, **(b)** July stratospheric zonal mean, **(c)** January NH troposphere (averaged over latitudes 35° N to 55° N), **(d)** July NH troposphere (averaged over latitudes 35° N to 55° N). In **(c)** and **(d)**, the three regions of enhanced tropospheric NO₂ represent, from left to right, the USA, Europe, and E. Asia, respectively.

[Title Page](#)[Abstract](#)[Introduction](#)[Conclusions](#)[References](#)[Tables](#)[Figures](#)[◀](#)[▶](#)[◀](#)[▶](#)[Back](#)[Close](#)[Full Screen / Esc](#)[Printer-friendly Version](#)[Interactive Discussion](#)

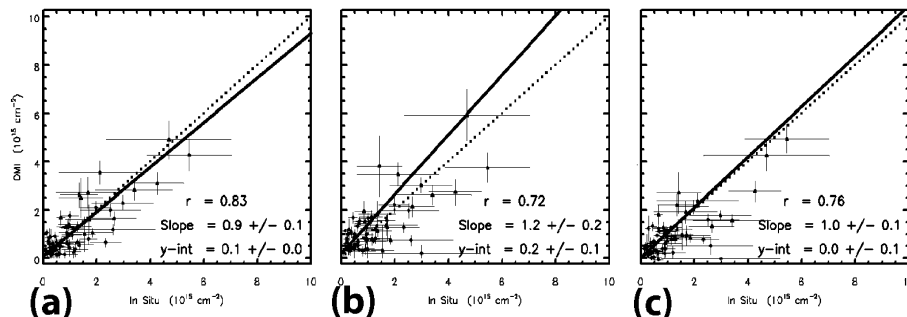


Fig. 9. Comparisons of tropospheric OMI NO_2 retrievals vs. integrated in situ LIF NO_2 measurements obtained during the INTEX-B field campaign over the Gulf of Mexico and clean Pacific locations. Shown are (a) SP1, but with collection 2 slant columns, (b) SP1 (current collection 3), and (c) SP2 (current collection 3). The solid line is an error-weighted least squares fit, and the dotted line is 1 : 1.

[Title Page](#)
[Abstract](#)
[Introduction](#)
[Conclusions](#)
[References](#)
[Tables](#)
[Figures](#)
[◀](#)
[▶](#)
[◀](#)
[▶](#)
[Back](#)
[Close](#)
[Full Screen / Esc](#)
[Printer-friendly Version](#)
[Interactive Discussion](#)
